

3-10-2010

Changes to Electrical Conductivity in Irradiated Carbon-Nickel Nanocomposites

David F. Coy

Follow this and additional works at: <https://scholar.afit.edu/etd>

 Part of the [Electromagnetics and Photonics Commons](#), [Inorganic Chemistry Commons](#), and the [Polymer Chemistry Commons](#)

Recommended Citation

Coy, David F., "Changes to Electrical Conductivity in Irradiated Carbon-Nickel Nanocomposites" (2010). *Theses and Dissertations*. 2179.
<https://scholar.afit.edu/etd/2179>

This Thesis is brought to you for free and open access by the Student Graduate Works at AFIT Scholar. It has been accepted for inclusion in Theses and Dissertations by an authorized administrator of AFIT Scholar. For more information, please contact richard.mansfield@afit.edu.



CHANGES TO ELECTRICAL CONDUCTIVITY IN IRRADIATED CARBON-NICKEL NANOCOMPOSITES

THESIS

David F. Coy, Major, USA

AFIT/GNE/ENP/10M-02

**DEPARTMENT OF THE AIR FORCE
AIR UNIVERSITY**

AIR FORCE INSTITUTE OF TECHNOLOGY

Wright-Patterson Air Force Base, Ohio

APPROVED FOR PUBLIC RELEASE; DISTRIBUTION UNLIMITED

The views expressed in this thesis are those of the author and do not reflect the official policy or position of the United States Air Force, Department of Defense, or the U.S. Government.

AFIT/GNE/ENP/10M-02

CHANGES TO ELECTRICAL CONDUCTIVITY IN IRRADIATED CARBON-
NICKEL NANOCOMPOSITES

THESIS

Presented to the Faculty

Department of Engineering Physics

Graduate School of Engineering and Management

Air Force Institute of Technology

Air University

Air Education and Training Command

In Partial Fulfillment of the Requirements for the
Degree of Master of Science in Nuclear Engineering

David F. Coy, BS

Major, USA

March 2010

APPROVED FOR PUBLIC RELEASE; DISTRIBUTION UNLIMITED

AFIT/GNE/ENP/10M-02

CHANGES TO ELECTRICAL CONDUCTIVITY IN IRRADIATED CARBON-
NICKEL NANOCOMPOSITES

David F. Coy, BS

Major, USA

Approved:

Dr. James C. Petrosky, PhD (Chairman)

Date

Dr. Larry W. Burggraf, PhD (Member)

Date

Dr. Shankar Mall, PhD (Member)

Date

Abstract

Pre and post irradiation resistivity and XAFS measurements have been conducted to examine the effects of 0.5 MeV electron irradiations on nickel-carbon composites. Results showed a decrease in surface resistivity in all sample types of 14-30% following irradiation with a total electron exposure of $4 \times 10^{16} \text{ cm}^{-2}$. Results also showed a corresponding decrease in NiO content for the irradiated samples as compared to measurements of non-irradiated samples. Surface resistivity measurement capabilities were established and measurement techniques refined to produce repeatable results of sufficient precision to discern changes in resistivity for an exposure of $2 \times 10^{16} \text{ cm}^{-2}$. Measured changes in surface resistivity were found to be consistent with previous studies of the radiation effects on electrical properties of polymers similar to the epoxies used in fabricating the composites studied here. Resistivity results also suggest that current flow close to the surface is a complex process not well modeled by simple Ohmic conduction. The materials examined showed surprisingly good radiation tolerance to 0.5 MeV electrons at total fluences up to $4 \times 10^{16} \text{ cm}^{-2}$. The data showed no discernable link between irradiation changes to surface resistivity and epoxy type used.

Acknowledgments

I would like to express my sincere appreciation to my faculty advisor, Dr. James Petrosky for his guidance and advice throughout this effort. I would also like to thank the Wright State University's electron beam staff for sacrificing a great deal of their time in helping me perform irradiations in the Van de Graaff facility. I would like to thank the many individuals at CAMD who assisted me and squeezed the most data out of a set of stubborn samples. I would also like to thank AFRL for assisting me in acquiring materials and test setups. Finally I would like to thank Conductive Composites Corporation for their excellent work on developing and fabricating the composite materials used in this investigation.

David F. Coy

Table of Contents

	Page
Abstract.....	iv
Acknowledgments.....	v
Table of Contents.....	vi
List of Figures.....	ix
List of Tables.....	xiv
List of Symbols and Acronyms.....	xvi
I. Introduction.....	1
1.1 Background.....	1
1.2 Objective.....	4
1.3 Paper Organization.....	5
II. Theory.....	6
2.1 Characterizing the Problem.....	6
2.1.1 The Space Environment.....	6
2.1.2 Nickel-Carbon Nanocomposites.....	9
2.1.3 Radiation Damage.....	10
2.2 Previous Research.....	14
2.2.1 Overview.....	14
2.2.2 Radiation Effects Research.....	14
2.2.3 EXAFS Research.....	17
2.3 Summary.....	18
III. Experiment.....	19
3.1 Experiment Overview.....	19

	Page
3.1.1 Experimental Focus.....	19
3.1.2 Materials Description	20
3.1.3 Sample Preparation	21
3.2 Surface Resistivity Measurements	25
3.2.1 Test Setup.....	25
3.2.2 Measurement Procedures	27
3.3 Bulk Resistivity Measurements.....	32
3.3.1 Measurement Setup.....	32
3.3.2 Measurement Procedures	32
3.3.3 Measurement Results	33
3.4 Sample Irradiations.....	34
3.4.1 Overview	34
3.4.2 Pre-Irradiation Calculations.....	35
3.4.3 Irradiation Procedures	38
3.4.4 Control Samples	39
3.5 XAFS Measurements.....	40
3.5.1 XAFS Overview	40
3.5.2 Measurement Setup.....	45
3.5.3 Measurement Procedures	47
3.5.4 Measurement Results	48
3.6 Experimental Summary	48
IV. Results and Analysis.....	50

	Page
4.1 Overview	50
4.2 Surface Resistivity Analysis.....	50
4.3 Bulk Resistivity Analysis	68
4.4 EXAFS Analysis	68
4.4.1 Summary	68
4.4.2 Data Processing.....	68
4.4.3 Theoretical Fits.....	70
V. Conclusions and Recommendations	74
Appendix A Pre-Irradiation Surface Resistivity Measurements.....	77
Bibliography	79

List of Figures

Figure	Page
Figure 1. Nickel nanotubes approximately 100 nm in diameter [3].	2
Figure 2. An illustration depicting the Van Allen radiation belts [7].	6
Figure 3. Solid line depicts the decrease in resistivity for a typical epoxy with the addition of nickel nanostrands TM [1].	10
Figure 4. Radiation tolerances of some thermoset resins. Light shaded region is moderate damage and dark shaded region is severe damage [17].	17
Figure 5. Panel of composite material with one inch disks and strip cut out. The strip was further cut into sticks for surfaced resistivity measurements. Disks were used for bulk resistivity and XAFS measurements.	22
Figure 6. Sticks used for surface resistivity measurements. Sticks were marked with a paint dot to distinguish sample number and side. Pictured from left to right are Ni-36-1, Ni-36-2, and Ni-36-3.	23
Figure 7. Disks for bulk resistivity measurements with aluminum circular contacts (left) and gold contacts (right).	24
Figure 8. Surface resistivity measurement setup.	25
Figure 9. Sample holder for surface resistivity measurements shown in the closed position.	26
Figure 10. Surface resistivity measurement sample IV data set and linear regression results.	28

Figure	Page
Figure 11. Sample in holder for surface resistivity measurements with sample placed to the far right, contacting the bolt.	30
Figure 12. Photo showing surface of a composite stick (left) and a graphite stick (right). Although the graphite stick has some texture, the surface appears much smoother than the composite stick.	31
Figure 13. Sample holder used for bulk resistivity measurements as viewed from the top and side.....	32
Figure 14. Best fit distribution for large sample set of bulk resistivity measurements. The 68% confidence interval is 84% of the average measurement value, thus changes to bulk resistivity were not distinguishable with this measurement method.	34
Figure 15. Results of CASINO [®] simulation showing electron penetration depth of 0.5 MeV electrons for a typical sample containing no nickel.....	35
Figure 16. Results of CASINO [®] simulation showing electron penetration depth of 0.5 MeV electrons for a typical sample containing nickel.....	36
Figure 17. Results of CASINO [®] simulation showing electron penetration depth of 1.0 MeV electrons for a typical sample containing nickel.....	37
Figure 18. Two sample sticks mounted on cold head for Van de Graaff irradiations. Copper wires and cellophane tape hold the sticks in place.....	39
Figure 19. Photon absorption coefficient for nickel as a function of photon energy. The step just below 10^{-2} MeV corresponds to the binding energy of K level electrons in nickel.....	40

Figure	Page
Figure 20. X-ray absorption for an isolated atom (a) and an atom with neighbors (b). For the atom in (a), the absorption coefficient decreases smoothly with increased energy beyond the absorption edge of a core electron. For the atom in (b), the wave function of the ejected electron backscatters off a neighbor atom and interferes with itself, modifying the absorption probability [22].	41
Figure 21. Schematic of XAFS setup for measurements in transmission mode. The beam travels from left to right, passing through the first ionization chamber where I_0 is measured, then through the sample where the beam intensity is attenuated, and finally through the second ionization chamber where I is measured.	43
Figure 22. Schematic of XAFS setup for measurements in fluorescence mode. The beam travels from left to right, passing through the first ionization chamber where I_0 is measured, then into the sample where X-rays are absorbed, then emitted as core electron vacancies are re-filled. The fluorescence signal is measured by a 13 element germanium detector placed 90 degrees from the incident beam.	45
Figure 23. Sketch of the CAMD DCM beamline. X-rays exit the synchrotron and traverse the beamline from left to right. The double crystal monochrometer, labeled DCM, is used to select X-ray energies used in the scan.	47
Figure 24. Absorption spectrum from a typical XAFS measurement, showing the absorption coefficient (dimensionless) as a function of photon energy.....	48
Figure 25. Surface resistance as a function of fluence for sample Ni-36-1.	54
Figure 26. Surface resistance as a function of fluence for sample C-36-2.	54
Figure 27. Surface resistance as a function of fluence for sample Ni-3-1.	55

Figure	Page
Figure 28. Surface resistance as a function of fluence for sample C-3-3.	55
Figure 29. Comparison of sample measurements to the Gaussian distribution for sample Ni-36-1 in the dot down orientation. The P-value of 0.2343 indicates a 23% probability the data came from the Gaussian distribution	56
Figure 30. Comparison of sample measurements to the Gaussian distribution for sample Ni-36-1 in the dot up orientation. The P-value of 0.0243 indicates a 2.4% probability the data came from the Gaussian distribution, thus the Gaussian distribution is rejected.	57
Figure 31. Best fit distribution for surface resistivity measurements of sample Ni 36 1 taken in dot down orientation. The P-value of 0.9826 shows a 98% probability the data matches the distribution.....	58
Figure 32. Profile views of samples Ni-36-1 (top) photographed with dot down, and C-36-2(bottom) photographed with dot up. The thickness (vertical in picture) of both samples is approximately 1 [mm]. Note the relative rougher surface of Ni-36-1, and the voids within its bulk.	61
Figure 33. Primary and secondary alkyl radicals as reported in reference [26]	63
Figure 34. Cross-linking reaction found after irradiation of polyester based polyurethane binder from reference [26]. Similar reactions may take place in the polyurethane binder used for the current research.	63
Figure 35. Absorption spectra for all the samples. From top to bottom the samples represented are Ni-36-4, C1, Ni-36-5, and C7. Samples Ni-36-4 and C1 were irradiated to $1 \times 10^{16} \text{ cm}^{-2}$, while the other two samples were not irradiated.	69

Figure	Page
Figure 36. XAFS spectra obtained from composite material published by Nietubyc et al. The top and bottom lines show NiO and Ni spectra respectively. The intermediate lines show results from samples with varying levels of NiO, from most (top) to least (bottom).....	70
Figure 37. XAFS data plotted in R-space.	71
Figure 38. Curve fitting results for sample Ni-36-4. Only the first shell was fitted.	72

List of Tables

Table	Page
Table 1. Baseline charged particle fluxes that geosynchronous satellites must withstand as established by MIL-STD-1809.	7
Table 2. Reported results for bulk resistivity before and after irradiation [4]	14
Table 3. Reported results for surface resistivity before and after irradiation [4].....	15
Table 4. Comparison of pre-irradiation and post-irradiation resistivity measurements for samples irradiated to $2 \times 10^{16} \text{ cm}^{-2}$. Relative change was estimated by taking the difference between the pre-irradiation average and the post-irradiation average. Note C-3-5 pre-irradiation values were measured as a large distribution and therefore the 68% confidence interval was used for the minimum and maximum values.....	51
Table 5 Comparison of pre-irradiation and post-irradiation resistivity measurements for samples irradiated to $4 \times 10^{16} \text{ cm}^{-2}$. Relative change was estimated by taking the difference between the pre-irradiation average and the post-irradiation average. Note C-3-3 pre-irradiation values were measured as a large distribution and therefore the 68% confidence interval was used for the minimum and maximum values.....	53
Table 6. P-test results of Gaussian fit for measurements taken of each sample type used.	59
Table 7. Measurement confidence window as a percentage of measurement average for each of the samples used and the graphite sample. Note that the graphite sample was not irradiated, so both values given are for non-irradiated configurations.	62

Table	Page
Table 8. Surface resistivity calculation results obtained using the infinite bar approximation and 68 % confidence windows for the best fit distributions.....	66
Table 9. Surface resistivity calculations using corrections derived from finite element analysis presented by Zimney et al. compared to calculations using infinite bar approximations. The minimum and maximum true resistivity values depend on the assumed bulk resistivity through the material. The lowest value was assumed to be 1.7 [mΩ-cm] corresponding to the resistivity of the carbon fiber. The maximum resistivity value was assumed to be those found in reference [4]. The lower bulk resistivity results in a larger correction factor and thus gives the maximum true resistivity in column 3.....	67
Table 10. Calculated contributions to the XAFS signal from each sample showing nickel, carbon, nickel-oxide, and nickel-hydroxide relative contributions.....	73
Table 11. Pre-irradiation surface resistivity measurement results showing resistance values averaged from 3 measurements and the corresponding standard deviations..	77
Table 12. Surface resistivity measurement results showing resistance values averaged from 20 measurements and 68% confidence interval from best fit distribution. Note, Ni-36, C-36, and Ni-3 samples were all measured after irradiation to $2 \times 10^{16} \text{ cm}^{-2}$.	78

List of Symbols and Acronyms

Å	Angstrom [10^{-10} meters]
A	Ampere measure of current
AFIT	Air Force Institute of Technology
C	Interwoven composite with 242 gsm Ni
CAMD	Center for Advanced Microstructure Devices
CASINO [®]	Monte Carlo Simulation of Electron Trajectories in Solids
cm	Centimeter [.01 meters]
DMM	Digital Multimeter
eV	Electron Volt
EMI	Electromagnetic Interference
ESD	Electrostatic Discharge
GEO	Geosynchronous Earth Orbit
gsm	Grams per square meter [references Ni content]
HDPE	High Density Polyethylene
<i>I</i>	Current [A]
IEC	International Electro-technical Commission
IV	Current verses Voltage
keV	Kilo Electron Volt [10^3 eV]
LSU	Louisiana State University
LTAPCVD	Low Temperature Atmospheric Pressure Chemical Vapor Decomposition
mA	Milliamp [10^{-3} A]

mΩ	Milliohm [10^{-3} Ohm]
MAJ	Major, U.S. Army
MeV	Mega Electron Volt [10^6 eV]
MIL-STD	Military Standard
μm	Micrometer [10^{-6} meter]
nA	Nanoamp [10^{-9} A]
NASA	National Aeronautics and Space Administration
Ni	Nickel
NiOH	Nickel Hydroxide
NiO	Nickel Oxide
NIST	National Institute of Standards and Technology
ORNL	Oak Ridge National Laboratory
torr	Measure of Pressure (vacuum) torr = 133.3 Pa
ρ	Resistivity [Ω -cm]
rad	Radiation Absorbed Dose
sec	Second
XAFS	X-ray Absorption Fine Structure
Ω	Resistance [Ω]

CHANGES TO ELECTRICAL CONDUCTIVITY IN IRRADIATED CARBON-NICKEL NANOCOMPOSITES

I. Introduction

1.1 Background

Ongoing efforts to develop and improve materials for all types of engineering applications include a diverse range of materials from plastics and ceramics to exotic alloys and carbon composites. Within those efforts, there is considerable interest in the development of conductive composite materials for applications where aluminum and other metals traditionally have been used, for example as structural components in satellites. In order to improve conductivity of carbon composites while maintaining their relatively high strength-to-weight ratio, Metal Matrix Composites Corporation has fabricated high aspect ratio nano-scale nickel filaments via Low Temperature Atmospheric Pressure Chemical Vapor Decomposition (LTAPCVD) which were subsequently mixed with polymers used to bind carbon composites. The resulting nickel-carbon nanocomposites showed high conductivity while remaining lightweight and durable [1]. An image of such nickel nanotubes, or nanostrandsTM, produced by Metal Matrix Composites Corporation is shown in Figure 1.

Because potential space applications would necessitate exposure to a radiation environment, the effects of radiation on the electrical properties of such conductive composite materials is of special interest. In particular, satellites in geosynchronous orbit are exposed to charged particles present in the radiation belts. At geosynchronous altitude energetic electron fluxes range up to $5 \times 10^6 \text{ cm}^{-2} \text{ sec}^{-1}$ for electrons with energies

of 0.5 MeV or greater, while proton fluxes for energies of 1 MeV or greater are on the order of $10^3 \text{ cm}^{-2} \text{ sec}^{-1}$ [2]. In the case of satellites, the charged particle fluxes contribute to both spacecraft charging and radiation damage, therefore it is important to know how a material conducts charge, thus reducing Electrostatic Discharge (ESD) effects, and how well a material can maintain its desirable electrical properties with the effects of permanent radiation damage.

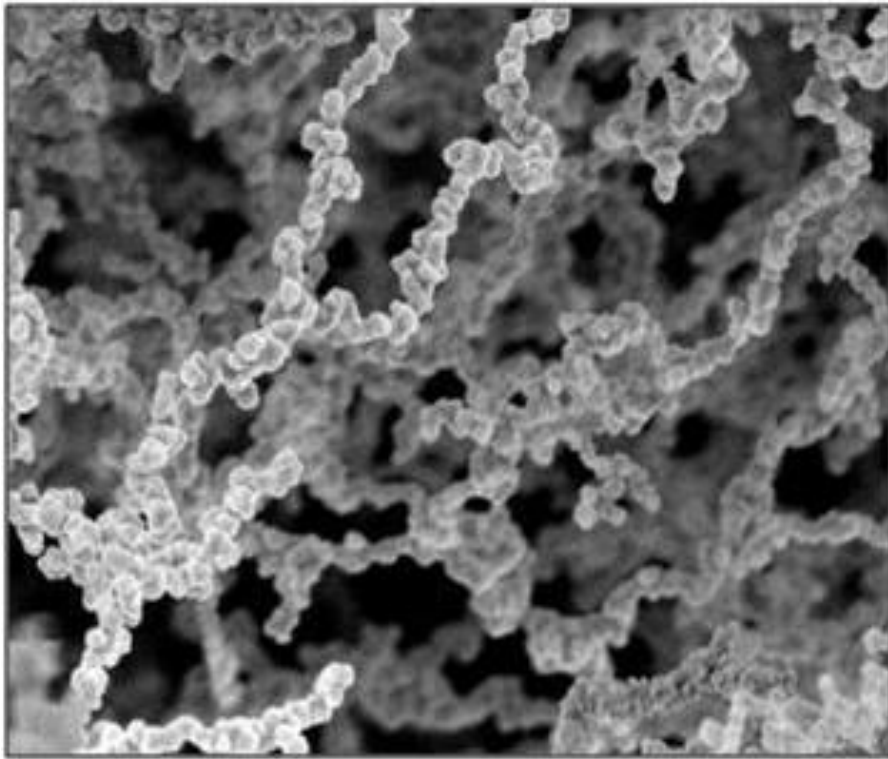


Figure 1. Nickel nanotubes approximately 100 nm in diameter [3].

One study of carbon-nickel nanocomposite electrical properties was conducted by previously at the Air Force Institute of Technology [4]. The investigation into the response of carbon-nickel nanostructures showed an interesting result as decomposition of the polymer binding the composite and subsequent chemical transformations of that

polymer appeared to dominate changes in bulk resistivity through the composite following irradiation. The results of that testing showed decreased bulk resistivity following irradiation for all samples containing polyurethane based epoxy, whereas all samples containing space grade epoxy increased in bulk resistivity following irradiation. All samples tested in [4] were reported to increase in surface resistivity following irradiation.

The changes to resistivity following irradiation presented in [4] were particularly interesting due to the different responses observed in surface and bulk measurements. Surface resistivity was found to increase following irradiation for all samples tested, while bulk resistivity increased for some sample types and decreased for other sample types. Bulk resistivity changes appeared to depend on the type of epoxy used to bond the composites, as it decreased for the samples made with polyurethane based epoxy and increased for those made with RS3 space grade epoxy. The reported different behaviors of surface and bulk resistivity in response to irradiation suggested that for the fluence levels used two separate mechanisms governed the composites' changes in resistivity at the surface and in the bulk. One proposed mechanism for the measured changes in bulk resistivity was dissociation of the epoxy polymer into free radicals which then would react chemically with other species in the material, thus altering some chemical properties. For the polyurethane based polymer the final result was a decrease in bulk resistivity while for the RS3 epoxy the result was an increase in bulk resistivity. It has been proposed that reactions at the surface, which may begin with similar dissociation, led to increased surface resistivity via the formation of nickel oxide (NiO) or nickel

hydroxide (NiOH) bonds [5]. The presence of NiO or NiOH would be expected to increase surface resistivity as both are known to be much more resistive than pure nickel.

1.2 Objective

The primary purpose of this investigation was to determine whether, for the nickel-carbon composites under investigation, the reported increases in surface resistivity following irradiation could be attributed to the formation of NiO or NiOH bonds.

Supporting purposes included verifying the reported behavior in material response to irradiation in terms of bulk and surface resistivity and examining the relationship between the types of epoxies used and their responses to irradiation.

The objectives of this work were as follows:

1. Establish surface resistivity and bulk resistivity test capabilities by fabricating test platforms and developing testing procedures that give consistent measurement results for comparison to previous work and follow-on experiments.
2. Measure surface and bulk resistivity of nickel-carbon nanocomposites before and after irradiation.
3. Identify the presence or absence of NiO and NiOH on sample surfaces in pre- and post-irradiation configurations and quantify the changes. Determine if a correlation exists between changes in surface resistivity and oxide presence.

1.3 Paper Organization

This thesis will address theory, experimental design, results and analysis, and provide conclusions and recommendations. The theory section will briefly describe the space environment as it applies to the issues of radiation damage and space vehicle charging and a description of the materials under investigation. For an in-depth analysis of the space environment and space vehicle charging refer to [4], which provides an excellent primer. The experiment section describes the design of the experiments used, the measurement setups and procedures, and provides relevant explanations of specialized measurement techniques. Pre-irradiation measurements will also be presented in the experiment section. The results and analysis section presents results of the post-irradiation measurements and analysis of those results. Finally the conclusions and recommendations section offers analysis of the outcome from the experiment and recommendations for follow-on research.

II. Theory

2.1 Characterizing the Problem

2.1.1 The Space Environment

As space applications are of primary interest for the nickel-carbon nanocomposites under investigation, a basic understanding of the environment in which the materials would be expected to perform provides some useful context for this research; therefore a brief description is presented here along with references to more detailed information. Satellites in geosynchronous orbit circle the earth approximately 35,000 km above the equator or 5.5 Earth radii, which places them in the outer Van Allen radiation belt [6]. The radiation belts are characterized by energetic charged particles – primarily protons and electrons – that are trapped in regions above the Earth by its magnetic field. An illustration of the Van Allen belts is provided in Figure 2.

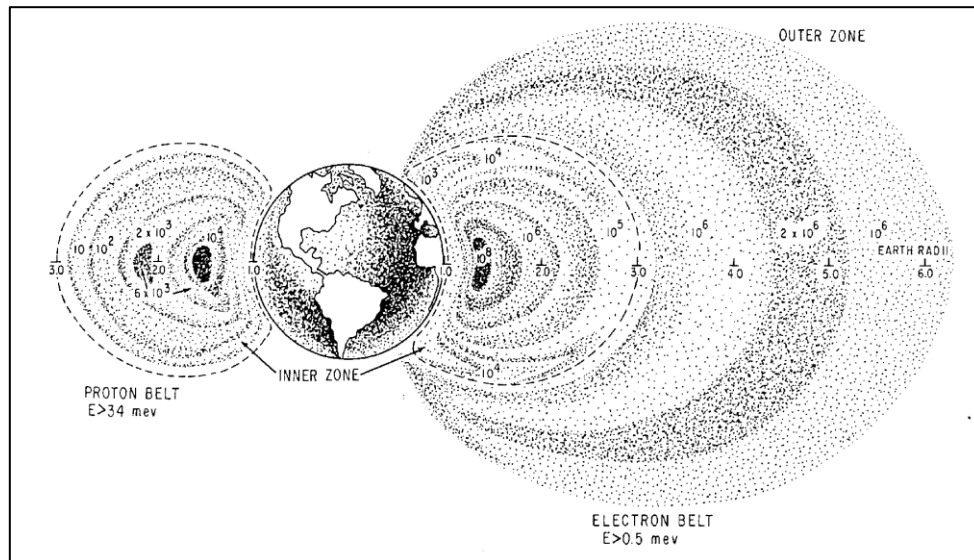


Figure 2. An illustration depicting the Van Allen radiation belts [7].

The energies and distributions of charged particles within the outer radiation belt vary with time and are influenced by such phenomena as geomagnetic storms. To provide a basis for assessing the tolerance of space systems to interactions with the environment, the U.S. Air Force has established a standardized definition which includes charge particle fluxes within which a space vehicle must be capable of operating. Those fluxes are higher than the expected actual space environment, but the definition provides an appropriate starting point for radiation fluences used when investigating radiation effects on the electrical properties of nickel-carbon nanocomposites, as any material considered for use in structural components on geosynchronous satellites should meet the criteria outlined in the standard. The baseline proton and electron fluxes defined in the military standard for geosynchronous orbit are listed in Table 1 [8].

Table 1. Baseline charged particle fluxes that geosynchronous satellites must withstand as established by MIL-STD-1809.

Proton Energy [MeV]	Flux [protons cm ⁻² sec ⁻¹]
> 0.1	1x10 ⁷
> 1	1x10 ³
Electron Energy [MeV]	Flux [electrons cm ⁻² sec ⁻¹]
> 0.1	2x10 ⁷
> 0.5	8x10 ⁶
> 1	2x10 ⁶
> 2	2x10 ⁴

For further details on the variability in the particle energies and fluxes in the space environment refer to the military standard MIL-STD-1809 or [2].

Exposing space vehicles to a flux of charged particles results in several effects that are important to the performance of structural components. The two effects considered in this investigation are spacecraft charging and radiation effects on electrical properties. Spacecraft charging will be discussed presently, while the discussion of radiation effects on electrical properties will be deferred until after a more complete description of the composite materials has been presented.

Spacecraft charging is essentially a buildup of charge density on a space vehicle surface leading to an unbalanced electric potential between the vehicle and the surrounding plasma or between separate surface regions or components of the vehicle itself. Uneven charge buildup can result from vehicle design combined with environmental conditions. Moreover, photoelectric effect and plasma bombardment are believed to contribute to spacecraft charging [2]. Uneven charges may build up as the vehicle or parts of the vehicle move into or out of sunlight or across magnetospheric boundaries to areas with higher or lower charged particle number densities [2]. The buildup of large static charges eventually leads to a discharge, known as ESD, which can cause permanent damage to satellite components. ESD can be either between satellite parts or between the satellite and the surrounding plasma. In order to reduce the uneven charge buildup across the satellite surface, conductive structural materials are preferred. This is evident in the fact that relaxation times are inversely proportional to conductivity,

that is, more conductive materials distribute charges more quickly. Therefore conductivity is an important property to consider for structural materials [9].

2.1.2 Nickel-Carbon Nanocomposites

The desire to develop suitable satellite shielding structures of even lighter weight than traditional aluminum shielding has provided the impetus to develop conductive composites. Carbon composites are fabricated in a number of ways and the composites under investigation for this project were formed by laying sheets of woven carbon fiber in a mold and pouring an epoxy into the mold to bind the layers together. The material is then compressed and heated. The resulting carbon composites are lightweight and exhibit good mechanical properties appropriate for use as satellite structural components [10]. While pure carbon exhibits good conductivity, less than 2 mΩ-cm for the fibers used in this investigation, the weak link in the overall conductivity of composites is the dielectric epoxy binding the layers of carbon. In order to increase conductivity in the epoxy, Metal Matrix Composites has employed many different techniques. For the samples investigated in this project, nickel nanostrandsTM were dispersed in the epoxy prior to fabrication, providing conductive pathways interspersed between carbon layers. In such a way, the resistivity of an epoxy is reduced by 5 orders of magnitude with the addition of 10% volume fraction of nickel, and the relatively high strength-to-weight ratio of a composite material can be maintained while improving conductivity between carbon layers. Figure 3 shows the effects of adding nickel nanostrandsTM to an epoxy as reported by [1].

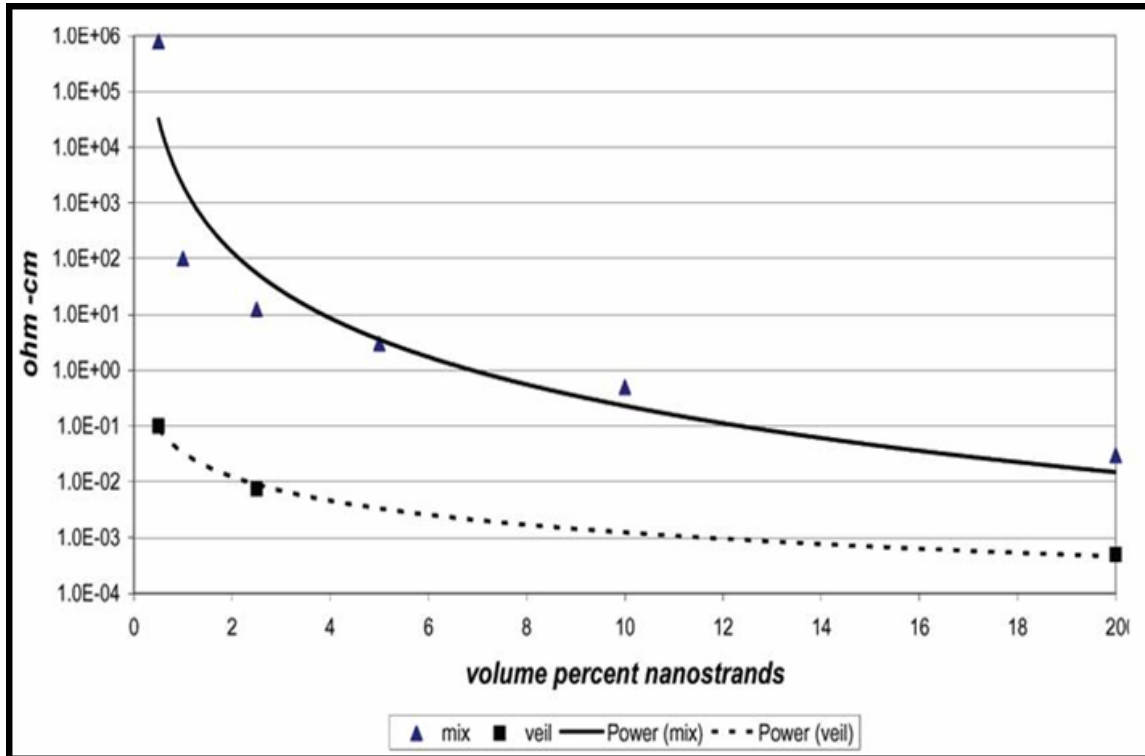


Figure 3. Solid line depicts the decrease in resistivity for a typical epoxy with the addition of nickel nanostrands™ [1].

2.1.3 Radiation Damage

The model proposed for changes in electrical properties of nickel-carbon nanocomposites subjected to radiation damage is a two part model in order to account for possible separate response mechanisms in surface and bulk resistivity. The theory behind each of those parts will be discussed separately, both in general and as applied to the specific composite material of interest.

Changes to bulk resistivity of the nickel-carbon composites are believed to be ruled by the response of the polymers to irradiation; therefore radiation chemistry of the polymers is of primary importance. In general the physical response of atoms to ionizing radiation is well understood. When charged particles such as electrons pass through a

material, energy is transferred to the material through Coulombic interactions and results in ionization and excitation. In addition to the primary interactions, high energy particles may transfer sufficient energy such that the electrons released during ionization can in turn cause additional ionizations. Such secondary electrons are called delta-rays, and the result of primary electron and delta-ray interactions is a network of scattering tracks filled with ionized and excited atoms and molecules. Gamma and X-ray effects are similar to small charged particle radiation effects. Gamma and X-ray interactions primarily consist of photo-electric absorption, Compton scattering, and pair production. From those reactions, energetic charged particles are liberated, and the liberated particles cause ionization and excitation in the same manner as described previously for primary electrons and delta rays [11][12].

Once atoms of a polymer become ionized or excited, neutralization and dissociation follow. It is dissociation into free radicals that is believed to dominate chemical changes in polymers following irradiation, and in fact inhibitors to conventional free radical reactions have been shown in many cases to reduce changes initiated by ionizing radiation [13]. Neutralization takes place primarily via two mechanisms, only one of which is expected to contribute to dissociation. The two mechanisms are ion-electron recombination and positive ion-negative ion interaction.

Ion-electron recombination takes place when a low energy or thermal electron encounters a positive ion. The Coulombic force brings the two together and results in an excited molecule with excitation energy equal to the ionization potential, on the order of

10 to 15 eV. As a result of the excitation energy, the molecule is likely to undergo further dissociation into free radicals, leading to permanent chemical changes [13].

Positive ion-negative ion interactions involve a charge transfer from the negative ion to the positive ion. This exchange may also result in excited states, but those states are not expected to be as energetic as in the case of ion-electron recombination, as some of the ionization potential of the gaining molecule is used in removing the electron from the negative ion. Therefore, dissociation and permanent changes are not as likely to occur.

The breaking of molecular bonds in polymers leads to two primary processes, scissioning and cross-linking. Scissioning of the long polymer chains leads to the formation of radicals which can then cause additional chemical reactions. In some cases the radicals create crosslinks linking one polymer chain to another. Scissioning results in changes to physical properties such as material softening and decreased tensile strength, while cross-linking leads to changes such as material hardening and increased tensile strength. It has also been noted in the study of failure mechanisms of irradiated dielectric polymers that permanent changes in electrical properties are usually small compared to changes in mechanical properties [14]. Therefore, dielectric polymers usually fail under irradiation due to physical deterioration well before changes to electrical properties compromise their performance. Previous research has shown that both scissioning and cross-linking take place in irradiated polyurethanes with neither process predominating the material response [14][15]. For instance [14] presents physical changes in polyurethane irradiated with 1 MeV electrons to a total fluence of $5.8 \times 10^{16} \text{ cm}^{-2}$.

The results showed a 67% increase in hardness (associated with cross-linking) and a 59% decrease in tensile strength (associated with scissioning). Similarly, reference [15] calculated a scissioning to cross-linking ratio for polyurethane of 1.2, with a cross-linking yield, $G(X)$, of $0.12 \pm 0.01 \times 10^{-7}$ moles/J and a scissioning yield, $G(S)$, of $0.14 \pm 0.01 \times 10^{-7}$ moles/J.

In the case of the nickel-carbon composites of interest, it is proposed that dissociation of the polymer into free radicals and the subsequent free radical reactions governs the changes in bulk resistivity following irradiation. The form of those reactions is as yet unknown. Because those reactions depend on the type of polymer and possibly on other materials present, it is expected that differences in bulk resistivity changes would be greater for composites having polymers of different types than for composites having polymers of the same type.


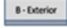
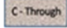


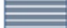
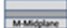
It has been proposed that changes to surface resistivity of the nickel-carbon composites could be ruled by the formation of Ni-OH or Ni-O bonds [5]. However, it will be shown that this investigation appears to invalidate this aspect of the radiation effects model. It was proposed that oxides, possibly released as polymers break down, could combine with nickel in nanostrands close to the surface, forming Ni-OH or Ni-O molecules. Ni-O can be up to four orders of magnitude more resistive than nickel, as both O, and OH have high electron affinities, greater than 2 eV. As a result, if a sufficient amount of Ni-OH or Ni-O formed near the surface, surface resistivity could be expected to increase following irradiation.

2.2 Previous Research

2.2.1 Overview

The results presented in [4] formed the starting point for this investigation and provided a basis to compare results for the radiation effects on electrical properties of nickel-carbon composites. Other studies of the radiation effects on polymers also provided a means for comparison of reactions in the epoxy. Additional studies of nickel nanoparticles embedded in carbon composites showed a means to compare X-ray

Table 2. Reported results for bulk resistivity before and after irradiation [4]

Configuration		Pre-Irradiation		Post Irradiation		Change
		Mean Resistivity	1- σ [Ω -cm]	Mean Resistivity	1- σ [Ω -cm]	%
A		1.40	0.15	1.15	0.12	-17.8
B		0.548	0.054	0.0689	0.0014	-87.4
C		0.215	0.037	0.0713	0.0094	-66.8
D		0.00684	0.00037	0.00798	0.00056	+16.5
Ext		0.0629	0.0098	0.0638	0.0099	+4.5
I		0.352	0.017	0.450	0.024	+27.3
M		13.2	0.672	14.9	0.81	+12.8





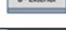


Absorption Fine Structure (XAFS) analysis of the surface following irradiation. Although the referenced XAFS measurements did not include radiation effects, the reported analyses of NiO and NiOH bonds present in nickel-carbon composites may be compared to post-irradiation measurements of similar materials that seek to identify the same chemical bonds.

2.2.2 Radiation Effects Research

The research in [4] used similar composite materials produced by Metal Matrix.

The focus was to determine whether the materials could meet military standards for space vehicle structural components before and after irradiation. Therefore the testing methods employed were based on military and commercial standards for ESD protection, primarily relying on MIL-STD-1809, on MIL-STD-1541(A) *Electromagnetic Compatibility Requirements for Space Systems*, and on International Standard IEC 801-2 for ESD testing. In [4] all samples were irradiated with a total electron fluence of $1 \times 10^{16} \text{ cm}^{-2}$ using 0.5 MeV electrons for an equivalent dose of $3 \times 10^8 \text{ rad(Si)}$. Those samples made with polyurethane based aero epoxy decreased in bulk resistivity by between 17.8 and 87.4%. Conversely, all samples made with RS-3 space grade epoxy increased in bulk resistivity by between 4.5 and 27.3%. Table 2 provides the results for bulk resistivity measurements from [4]. The samples in configurations A, B, and C all contained aero epoxy. All other samples were made with RS-3. The most interesting aspect is the percent change in the last column; all aero epoxy composites decreased in bulk resistivity following irradiation.

Table 3. Reported results for surface resistivity before and after irradiation [4].

Configuration		Pre-Irradiation		Post Irradiation		Change
		Mean Resistivity	1- σ [m Ω -cm]	Mean Resistivity	1- σ [m Ω -cm]	%
Ext		20.0	± 0.2	108	± 1.0	+440
D		10.6	± 0.3	37.2	± 1.9	+250
M		12.5	± 1.2	38.9	± 1.9	+211
I		13.9	± 0.1	35.1	± 1.8	+152
B		22.9	± 0.5	49.5	± 2.5	+116
C		25.6	± 1.8	45.3	± 2.3	+76.9
A		30.3	± 0.8	44.0	± 2.2	+45.2

In contrast to the bulk resistivity results, all samples tested in [4] increased in surface resistivity by between 45.2 and 440%. Table 3 shows the results for surface resistivity measurements presented in [4]. The samples in configurations A, B, and C all contained aero epoxy, and the rest contained RS-3. Samples used in [4] had many different configurations and levels of nickel content, possibly contributing to the variance in resistivity changes within each epoxy class.

Additional research with similar conductive composites was reported in reference [10]. The measurements performed in that research focused on changes to material properties following irradiation, but also included some resistivity measurements useful for comparison. The results of mechanical testing showed an increase in tensile strength of 22% for one sample following irradiation to $1 \times 10^{14} \text{ cm}^{-2}$ with 1.2 MeV electrons. Such an increase in tensile strength is indicative of cross-linking within the polymer binder.

Other radiation effects experiments on polymers can provide means for comparison as the role of polymer change may be dominant. Dose level dependence on polymer degradation provided a good basis for comparison. Tests conducted by Sisman and Bopp at Oak Ridge National Laboratory (ORNL) in 1952 showed permanent decreases in volume resistivity for polyethylene sheets subjected to total doses greater than 10 krad [13]. Similarly, results reported by Van de Voorde of CERN showed moderate to severe degradation of polyurethane rubber at doses of approximately 10^9 rad [16]. Additional data was found in CERN and NASA reports in which the mechanical degradation of polyurethane and epoxies were reported as functions of dose [17][18][19].

Those reports provided some comparison to measurements of resistivity changes as a function of dose, as changes in mechanical properties are to some extent correlated with changes in electrical properties. Figure 4 shows some of the data from CERN report 98-01. Note that the variation in tolerances for the different polymers spans several orders of magnitude.

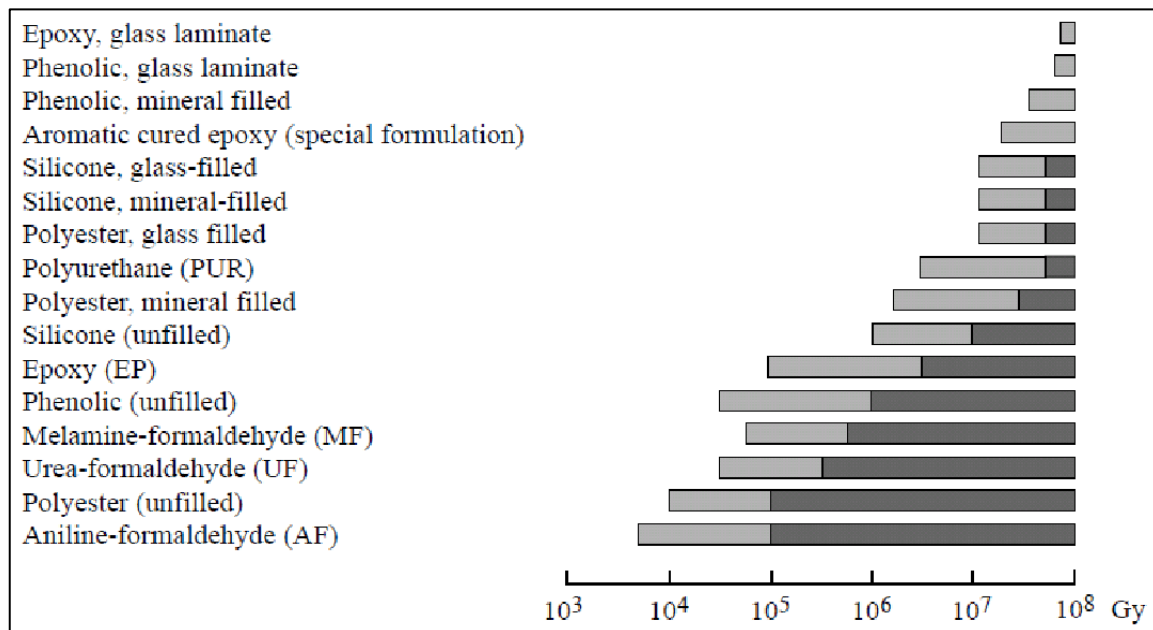


Figure 4. Radiation tolerances of some thermoset resins. Light shaded region is moderate damage and dark shaded region is severe damage [17].

2.2.3 EXAFS Research

In addition to the previous work on polymers, work on similar composite materials provides useful data for comparison. Two published works are of great interest to this investigation. The first work, published by Ushiro et al., focused on identifying Ni bonds present as an artifact of the manufacturing process for nanocomposites and on

identifying the resulting bond structures and lengths. Their testing relied upon XAFS analysis in combination with multiple scattering calculations to identify the bonds present in their test materials. The published results of their work included XANES spectra for various reference materials, and from those spectra Ni-Ni, Ni-O, and Ni-C bond lengths and standard XAFS parameters have been extracted [20]. The second work focused on using fitting coefficients derived from multiple XAFS spectra to measure changes in oxide content of Ni nanoparticles [21]. Those results may be compared to XAFS data for irradiated nanocomposites to aid in identifying Ni-O or Ni-OH bonds that may be present before or after irradiation.

2.3 Summary

The space environment as defined in MIL-STD-1809 in conjunction with the work from [4] and others provided a starting point for selecting materials, choosing irradiation levels for testing, and deciding on specific measurement techniques to employ in this investigation. The radiation tolerances that satellite structural materials must meet provided a good starting point for irradiation levels to investigate. Results from [4] also provided insight into which materials might provide the most insightful responses and the magnitude of changes to be expected. As the following sections will show, the changes measured in this investigation were considerably smaller than previously reported. Previously reported XAFS data demonstrated the utility of that measurement technique in identifying NiO and NiOH bonds on the surfaces of materials and could be extended to include post-irradiation conditions.

III. Experiment

3.1 Experiment Overview

This experiment measured the radiation response in surface resistivity of four types of carbon composites, then explored the potential correlation between resistivity and the formation of NiO or NiOH bonds. The four sample types included two with nickel nanostrands and two without. The samples were further divided into two types, one type fabricated with polyurethane based epoxy and one type fabricated with a space grade epoxy. Surface and bulk resistivity measurements were conducted and samples were irradiated with 0.5 MeV electrons using a Van de Graaff generator. Post-irradiation resistivity measurements were performed, and XAFS spectra were acquired.

3.1.1 Experimental Focus

In order to achieve the objectives of this research, three separate but interrelated irradiation material responses were examined: surface resistivity changes, bulk resistivity changes, and oxide formation. The experimental model focused on limiting the number of variables measured and establishing measurement methodologies that provided consistent and clear results. As will be discussed in the following section, that effort was successful for surface measurements but not for bulk measurements.

The experiment focused on four different sample types, of which two sample types were bonded with RS-3 space grade epoxy and two types were bonded with RS-36 epoxy. Within each epoxy type, two samples contained nickel and two did not. The four sample types were labeled Ni-36, C-36, Ni-3, and C-3. The labels indicate the sample composition so that samples labeled Ni-36 came from a single sheet of composite

material containing nickel and bonded with RS-36 polyurethane based epoxy. Samples labeled with C contain only carbon and epoxy (no nickel), and sample types labeled with a 3 have been bonded with RS-3 space grade epoxy. Each sample type has a relationship of one common variable and one dissimilar variable with two of the other three sample types, where the variables used are nickel content and epoxy type. By measuring the surface and bulk resistivities before and after irradiation, one can test whether the relative changes in resistivity are more closely related within the samples made with the same epoxy type or with the same nickel content to determine if nickel content or epoxy type plays the greater role in changes to surface and bulk resistivity.

3.1.2 Materials Description

All samples were fabricated based on sample type C from [4], which contained nickel nanostrands throughout the sample volume. Each sample type was fabricated as a single composite panel approximately 18 x 13 x 1 mm, from which individual test samples were cut. The panels were fabricated by layering 6 sheets of AS4 woven carbon fiber, then bonding with either RS36 polyurethane based aero grade epoxy or RS-3 space grade epoxy. Samples containing nickel nanostrandsTM were fabricated by first dispersing the nanostrandsTM in the epoxy. The target density for nickel was 242 gsm.

This sample type was chosen so that nickel would be present on and near the surface as required for XAFS measurements intended to identify NiO or NiOH bonds, while also ensuring nickel content would not be significantly different between the surface and the interior. The second consideration was intended to reduce the number of

variables in material type so that relative changes to bulk and surface resistivity could be compared to each other, an especially important consideration as previous results showed cases of increased surface resistivity and decreased bulk resistivity in the same sample types following irradiation.

3.1.3 Sample Preparation

Once panels of each material type were obtained, individual test samples were cut into bars or sticks approximately 20 x 2 x 1 mm for surface resistivity measurements and into one inch diameter circular disks for bulk resistivity and XAFS measurements.

Figure 5 shows a typical panel with disks and a strip cut out. The one inch diameter disks were cut using a high precision water jet. For cutting, the panels were prepared by taping a piece of plastic to each of the panel faces to reduce the potential for delamination. The water jet was used to cut the one inch diameter disks and to cut a strip of material 20 mm wide from each panel that could then be cut into sticks for surface measurements. The sticks were cut to the desired width using a table top diamond saw. Figure 6 shows three sticks used for surface resistivity measurements.

The sample dimensions and preparation procedures were chosen to follow as closely as possible to those reported in [4] in order to reduce the probability of introducing changes that may affect measurements and to allow for the most direct comparison to previous results; however, some changes were introduced and will be addressed in the following paragraphs. One inch diameter disks and stick dimensions were chosen to mirror those used in [4] and enable use of the same type of bulk and surface resistivity measurement setups which included fixtures that restrict the maximum

sample sizes that could be measured. Moreover, the beam area for the electron beam from the Van de Graaff also limited the maximum useful sample size to a one inch diameter.

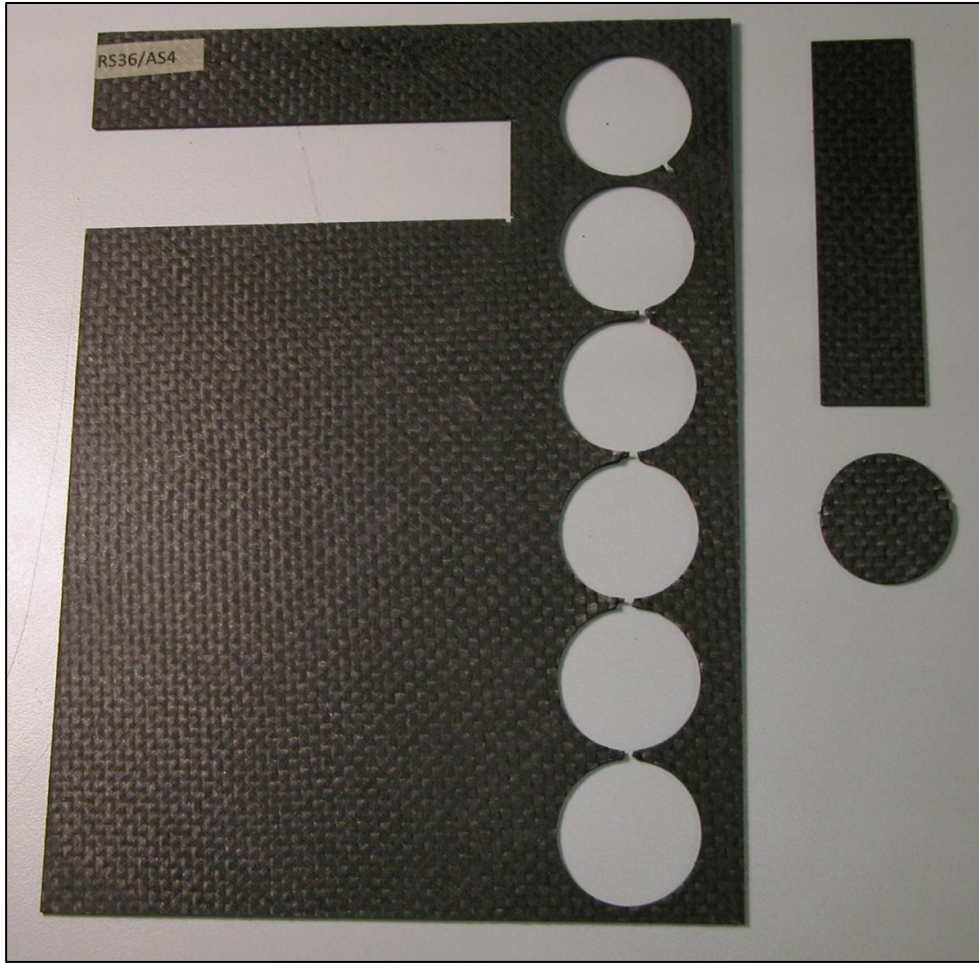


Figure 5. Panel of composite material with one inch disks and strip cut out. The strip was further cut into sticks for surfaced resistivity measurements. Disks were used for bulk resistivity and XAFS measurements.

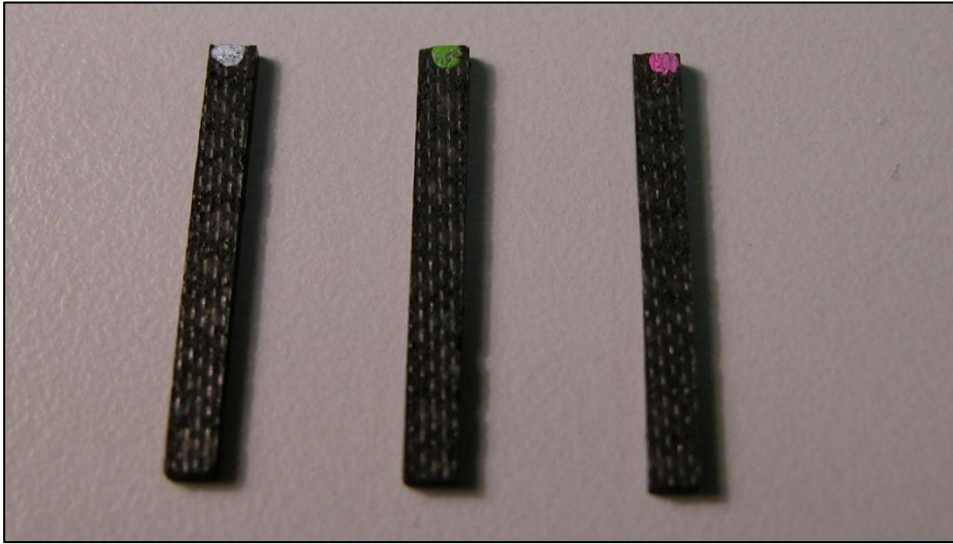


Figure 6. Sticks used for surface resistivity measurements. Sticks were marked with a paint dot to distinguish sample number and side. Pictured from left to right are Ni-36-1, Ni-36-2, and Ni-36-3.

Following cutting, electrical contacts were deposited onto the disk samples to reduce contact resistance for the bulk resistivity measurements. The contacts were all 200 Å thick, with aluminum used on the slotted side and gold used on the opposite face as depicted in Figure 7.

The first departure from previous work in terms of sample preparation was the mounting method used when cutting sticks with the diamond saw. The method previously employed was to use a wax melt to fix the sample onto a strip of graphite, with the graphite fixed to an aluminum base plate, and the base plate in turn clamped to the holder arm of the diamond saw. The graphite served as an expendable buffer material for the saw. After cutting, samples were heated to approximately 135° C to melt the wax and remove the sticks from the mounting base. While the samples were hot, excess wax was also absorbed from the samples using paper towels. This same method of wax

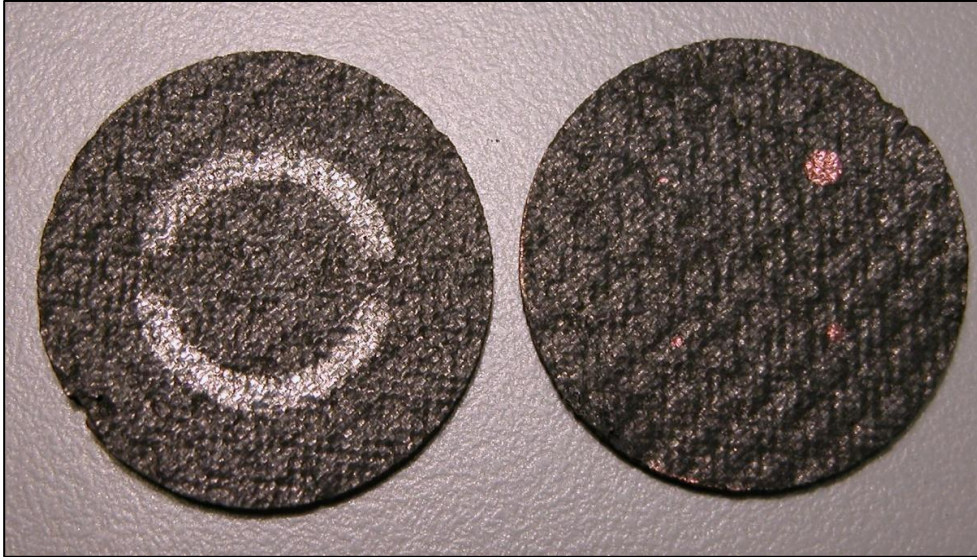


Figure 7. Disks for bulk resistivity measurements with aluminum circular contacts (left) and gold contacts (right).

mounting was used initially for cutting samples to be used in the current investigation; however, the surface resistivity measurements showed a large variability, which was believed to be an effect of incomplete wax removal. The decision was made to use standard masking tape to fix the samples to the cutting base. The minor tape residue was easily removed using alcohol swabs, and the sample measurements were much more consistent. Pre-measurement testing was also conducted to evaluate cleaning methods. Sticks were cleaned with methanol, isopropyl alcohol, and hexane. No differences were found between measurements taken with the three different cleaning techniques. Isopropyl alcohol was selected as the standard cleaner due to its ease of use.

3.2 Surface Resistivity Measurements

3.2.1 Test Setup

Surface resistivity measurements were taken using a four point parallel probe setup connected to a Keithley 4200 Semiconductor Characterization System (SCS).

Figure 8 shows the high density polyurethane (HDPE) sample holder with four parallel gold tipped probes (on right) and the sample holder inside the aluminum enclosure (on left).

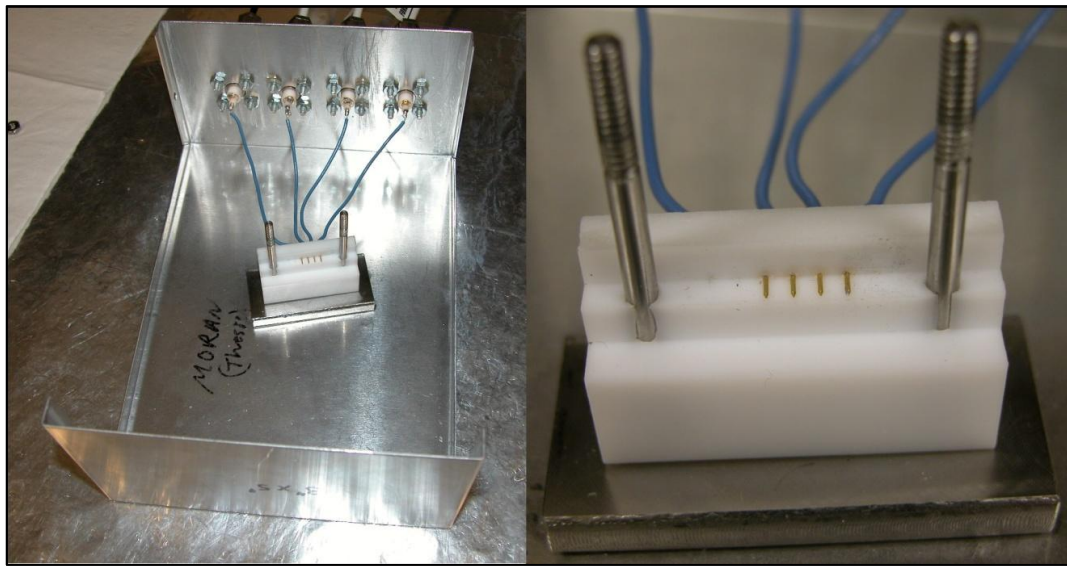


Figure 8. Surface resistivity measurement setup.

While taking measurements, the top was placed on the aluminum enclosure which served as a Faraday shield to reduce electromagnetic interference. Wires connected to the four probes were soldered to four triaxial connectors, which were connected to the source measurement units of the Keithley 4200 SCS via 7078-TRX-10 low noise triax

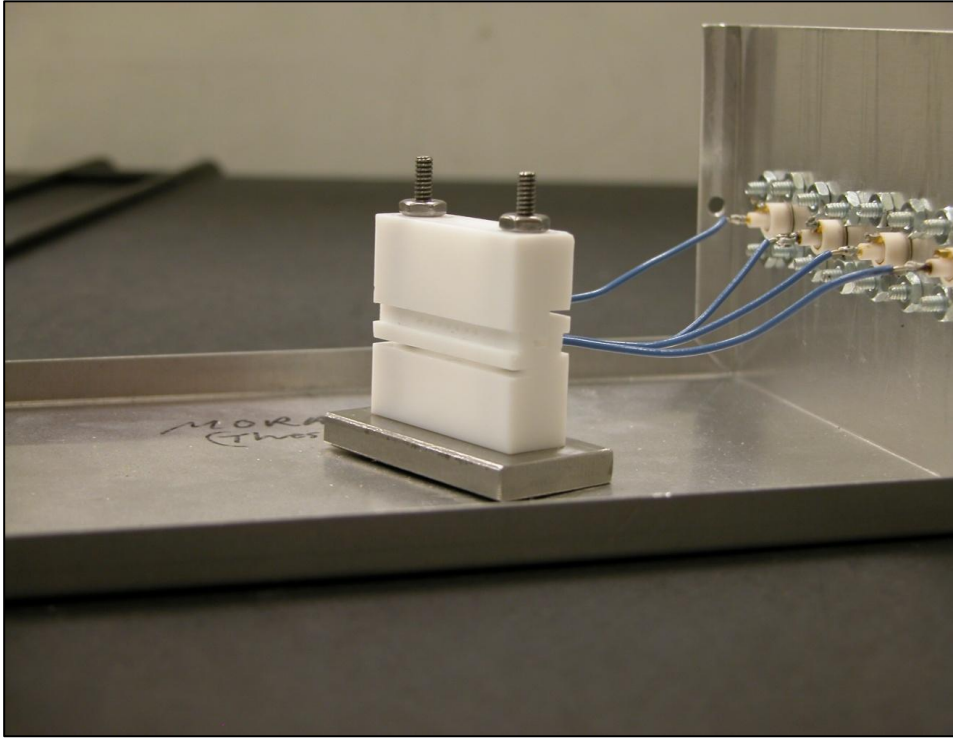


Figure 9. Sample holder for surface resistivity measurements shown in the closed position.

cables. To take measurements, a sample stick was placed on the probes, which were designated 1 to 4, and the top of the sample holder closed and tightened finger-tight with two retaining nuts. Figure 9 shows the sample holder in the closed position.

The lid was placed on the aluminum enclosure, and the measurement was performed by sourcing current through probe 1 and measuring the voltage at probes 2 and 3. Probe 4 was connected to ground. The current injected at probe 1 was stepped from -10 to $+10$ mA in 2 mA steps, holding the current for 3 seconds at each step to reduce transient effects. With the current across the sample known, the voltage drop across probes 2 and 3 were calculated and the resistance determined from Ohm's Law as shown in Equation 1.

$$R = \frac{\Delta V}{\Delta I} \quad (1)$$

3.2.2 Measurement Procedures

Surface measurements were performed as follows. The sample was first thoroughly cleaned using isopropyl alcohol and allowed to dry. Next, the sample was placed into the sample holder, centered in the holder so as not to contact either of the two bolts along the sides. The sample holder was then closed and the retaining nuts were tightened to finger tight, finally the lid was placed on the aluminum enclosure. The Keithley 4200 SCS was used to acquire current-voltage (IV) measurements from -10 to +10 mA using the Keithley Interactive Test Environment (KITE). The IV data were plotted as shown in Figure 10, where current is plotted along the x-axis and the voltage drop between probes 2 and 3 is plotted along the y-axis. A linear regression was performed and the slope of the regression line was recorded as the resistance measurement of the sample. After the resistance was recorded, the sample was removed from the holder, turned over, and placed into the holder to measure the opposite face. Each sample was initially measured three times on each face and the average measurement taken as the point estimate for the resistance value.

Following irradiation, surface resistivity measurements were repeated as described above; however the results highlighted a need for more precise confidence intervals and the resistivity measurement procedures were adjusted. Analysis of the results will be discussed in detail in Chapter IV. In brief, it was found that the changes in surface resistivity were much smaller than those reported from previous work and were

on the order of variances noted in the three measurements taken for many of the samples. Therefore, it became necessary to take additional measurements of each stick to determine a distribution associated with that measurement and to determine the 68% confidence interval for each measurement. 20 measurements of each sample type were acquired.

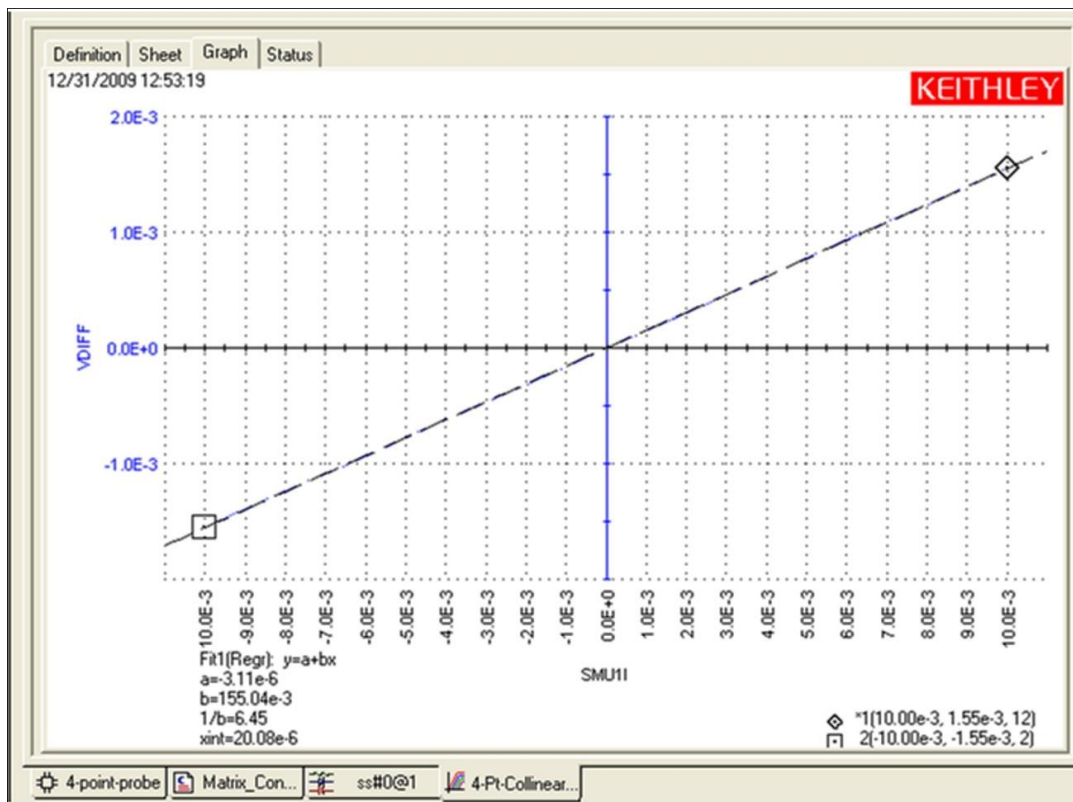


Figure 10. Surface resistivity measurement sample IV data set and linear regression results.

Two important factors were noted while taking surface resistivity measurements that directly affect measurement precision and repeatability. First, the opposite sides of each stick gave a different resistance value and different variance in measured values. This was expected as the fabrication process results in slightly different surface roughness and epoxy quantities on each face of the panel. Similarly, different

measurement values were expected for each face in post-irradiation measurements as the majority of electron energy was deposited in the side of the sample facing away from the electron beam. Therefore, each stick was marked with white, green, or pink dots, and the sample was always placed in the holder with the dot on the left hand side. It was also noted which way the sample was placed in the holder, e.g. with dot up or dot down.

The second factor of note was that samples should be removed from the sample holder and re-measured for each of the 20 measurements. Taking multiple measurements without removing and re-inserting the sample would give a much smaller range of values that are indicative of the precision of the Keithley 4200 SCS for the given configuration. Both types of measurements were taken for comparison. The measurements taken without removing the sample followed the expected Gaussian distribution. On average those 20 measurement sets showed a standard deviation of 0.1 m Ω , or less than 1% of the measured resistance for each sample. Thus the measurement precision was taken as 0.1 m Ω . However, the uncertainty associated with the point estimate for the resistance of one side of each stick was much greater. That uncertainty ranged from 2.55 to 20%. This variability was attributed to a combination of factors that included imprecise placement of the sample stick in the center of the holder, variability in surface roughness, and non-homogeneous distribution of materials in the composites. A more detailed discussion of these factors will be provided in Chapter IV Results and Analysis.

Three additional surface measurements were used for comparison to the primary measurements described previously. The first was conducted by placing the sample in the holder as far to one side as possible, so as to contact the bolt on that side. This method, shown in Figure 11, was not initially desired due to the potential for the bolt to provide an alternate conductive path to ground and thus change the measurement.

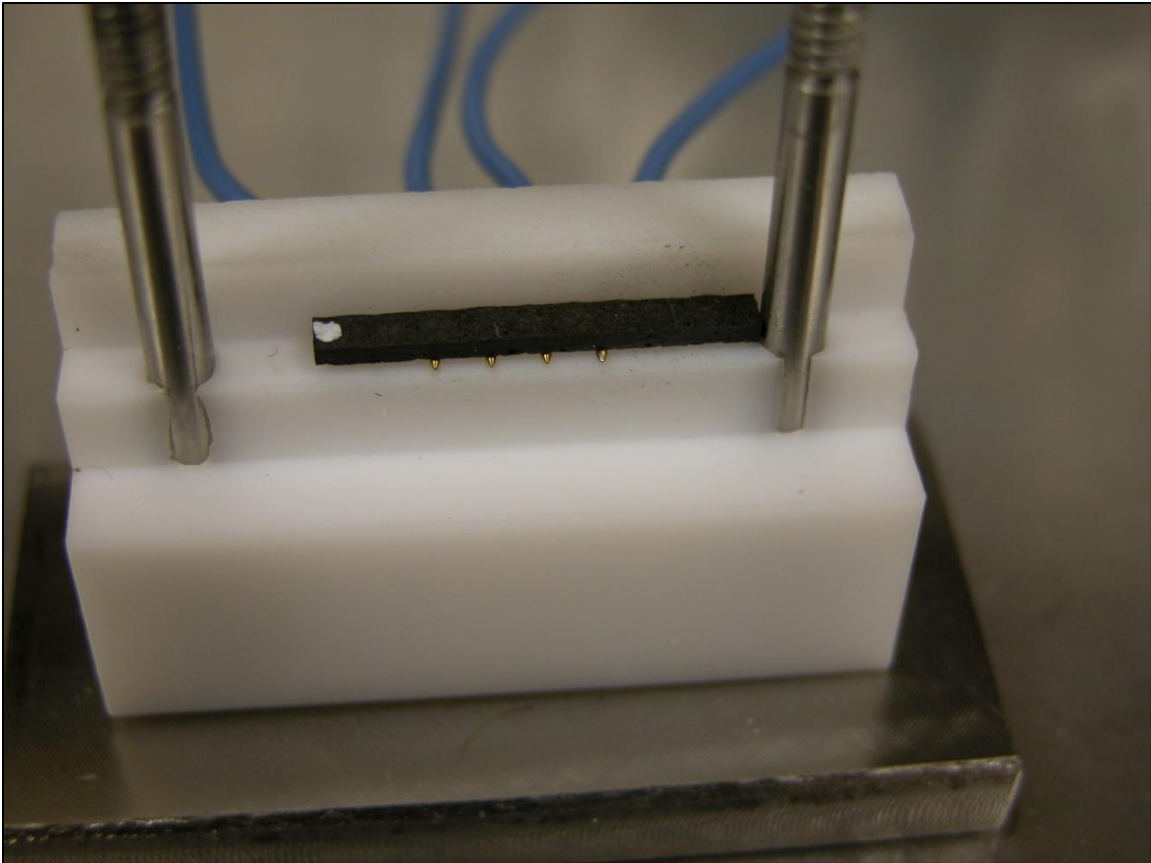


Figure 11. Sample in holder for surface resistivity measurements with sample placed to the far right, contacting the bolt.

Although the values did change for the sample tested, the variation in measured resistance for that data set was approximately 47% smaller than the data acquired with the same sample placed in the center of the holder. The second additional test was

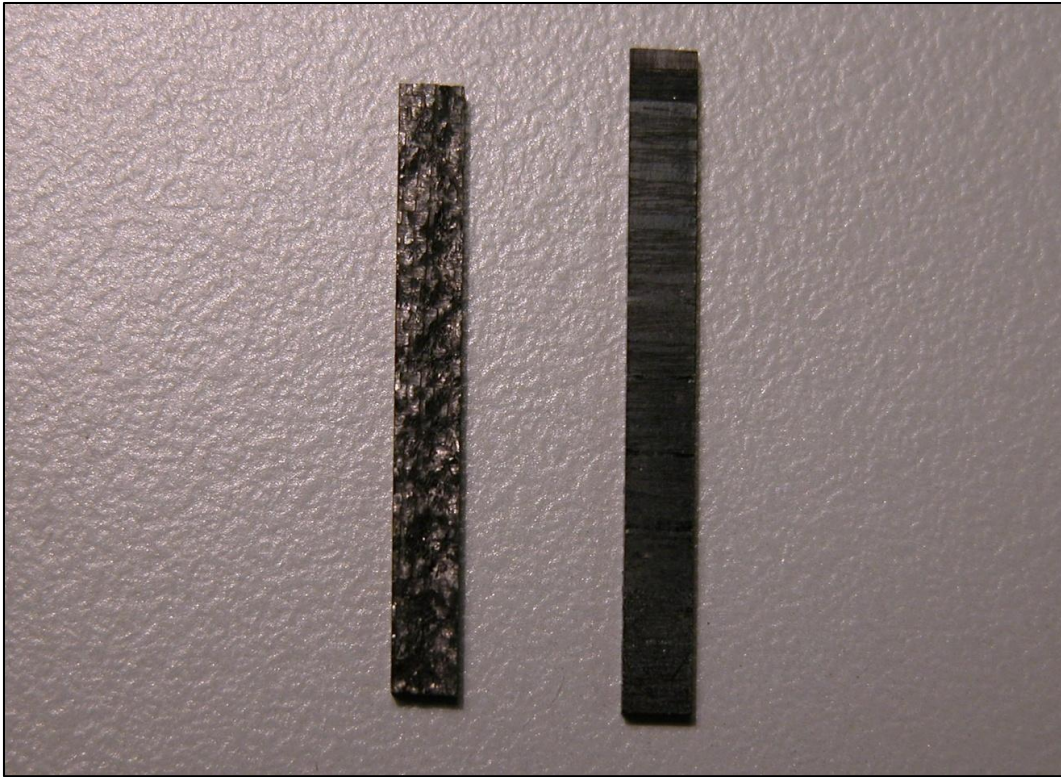


Figure 12. Photo showing surface of a composite stick (left) and a graphite stick (right). Although the graphite stick has some texture, the surface appears much smoother than the composite stick.

conducted using a graphite sample. The graphite sample, pictured on the right side in Figure 12, had a smoother surface than the typical composite sample and was therefore expected to show less variability in measurement value. The third additional test was a measurement of sample EXT 1 from reference [4]. Although tests were conducted on many of the samples from reference [4] to ensure the surface measurement setup would provide comparable results, none included a large data set of 20 points for one sample.

Once the need for sample distributions was recognized, a large set of measurements was collected using sample EXT 1.

3.3 Bulk Resistivity Measurements

3.3.1 Measurement Setup

Bulk resistivity measurements were conducted as described in [4], based on the IEC 801.2 standard, using a one pound stainless steel compression weight. To stabilize the compression weight, a sample holder was used that consisted of a hollow high density polyethylene (HDPE) cylinder with a copper base plate. Figure 13 shows the sample holder.

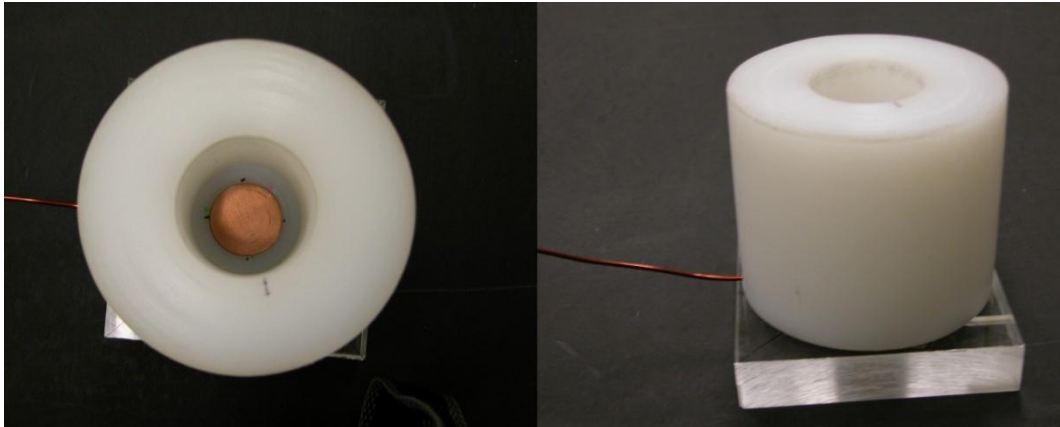


Figure 13. Sample holder used for bulk resistivity measurements as viewed from the top and side.

3.3.2 Measurement Procedures

Bulk resistivity measurements were taken by placing the sample onto the copper base inside the HDPE cylinder with the aluminum contact facing up. The sample was aligned using a paint dot placed on the disk and dots placed in the bottom of the sample holder. With the sample aligned, the stainless steel compression cylinder was lowered

slowly onto the sample. Four wire probes were connected to the top of the compression weight and to the copper wire then connected to a Keithley 2700 digital multimeter. Resistance measurements were conducted using a four wire method similar to the four wire method used in surface measurements; however, in the bulk measurements the voltage drop was measured across the sample bulk versus along the surface.

3.3.3 Measurement Results

Bulk resistivity measurements showed inconsistent results, despite taking several steps to reduce the variation. First, larger compression weights were used, including 1 kg, 5 lb, and 10 lb weights. Second, gold foils were placed between the sample and the compression weight and between the sample and the copper plate. The malleable gold foils provided a better contact at the interfaces and reduced the magnitude of the measurements by nearly a factor of 10, but there was still a significant variation in the measurements. Third, the copper base plate was changed from its original position in which it was allowed to float in terms of its angle with respect to the sample surface. Fixing the base plate provided no noticeable improvement. Finally, one large measurement sample was collected for sample disk Ni-3-3 to determine if statistical methods would provide sufficient confidence to determine post-irradiation changes in the measurements. The measurements are summarized in the distribution analysis shown in Figure 14. From the results it is apparent that the confidence interval is too broad to discriminate changes that resulted following irradiation.

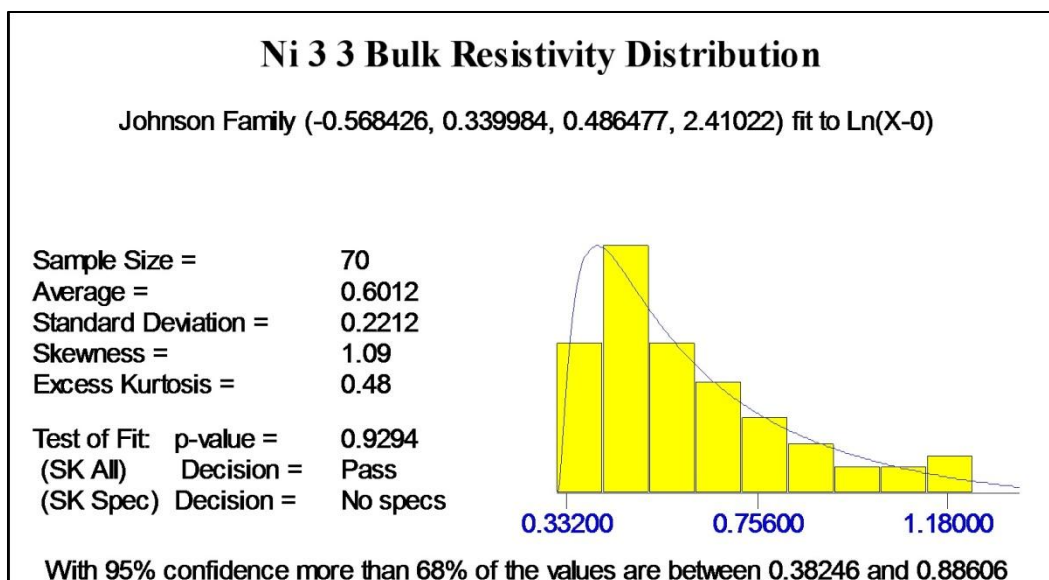


Figure 14. Best fit distribution for large sample set of bulk resistivity measurements. The 68% confidence interval is 84% of the average measurement value, thus changes to bulk resistivity were not distinguishable with this measurement method.

The sample set also failed the P-test with 98% confidence, meaning it is unlikely the data came from a Gaussian distribution. Statistical testing criteria will be addressed more fully in the results and analysis section.

3.4 Sample Irradiations

3.4.1 Overview

Electron irradiations were conducted at Wright State University's Van de Graaff facility. Irradiation levels were selected to cover a range of electron fluences below and above those used in previous work. For all irradiations, an average electron energy of 0.5 MeV was used for comparison with previous work and because CASINO[®] electron simulations indicated a large fraction of the electron energy would be deposited within

the sample for 0.5 MeV electrons. Irradiation levels used were as follows: 5×10^{15} , 1×10^{16} , 2×10^{16} , and $4 \times 10^{16} \text{ cm}^{-2}$.

3.4.2 Pre-Irradiation Calculations

Pre-Irradiation calculations were conducted to verify the appropriateness of the energy range and to ensure the correct fluence would be applied for each irradiation. Electron energy deposition was predicted using CASINO[®] electron code, results of which are depicted in Figures 15 through 17. The three figures show electron penetration depth

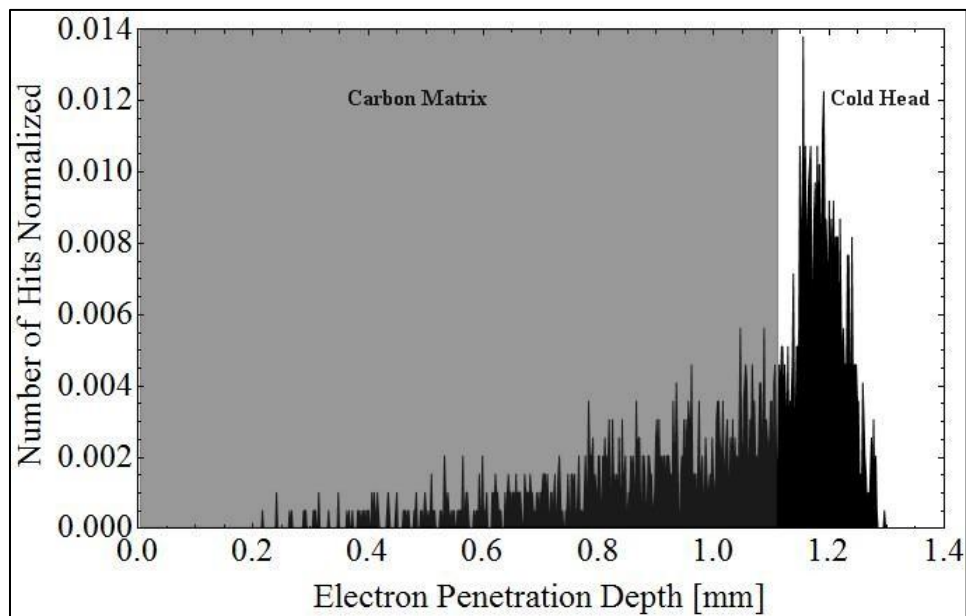


Figure 15. Results of CASINO[®] simulation showing electron penetration depth of 0.5 MeV electrons for a typical sample containing no nickel.

for electrons. Note that the penetration depth is the stopping point for simulated electrons and most of the electron energy is expected to be deposited in the final 10% of its range.

Therefore the energy distribution would be spread-out slightly to the left of the

penetration depth depicted in Figures 15 through 17. Figure 15 shows results for a carbon only sample, i.e. no nickel content, and Figure 16 shows results for a nickel-carbon composite. Both simulations indicated that a large fraction of the electron energy would be deposited in the samples.

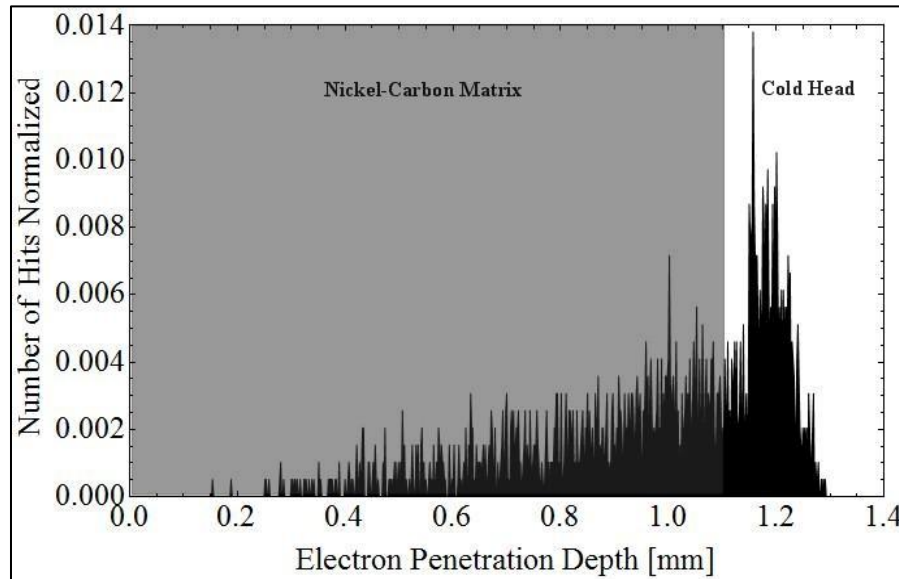


Figure 16. Results of CASINO[®] simulation showing electron penetration depth of 0.5 MeV electrons for a typical sample containing nickel.

In contrast to the first two CASINO[®] results, Figure 17 shows the penetration depth of 1.0 MeV electrons. As the figure shows, most of the electron energy would be deposited in the aluminum cold head on which the samples were mounted. The three simulation results confirmed the selection of electron energy at 0.5 MeV and reinforced the expectation that most of the transferred electron energy would be deposited in the sample side facing away from the electron beam.

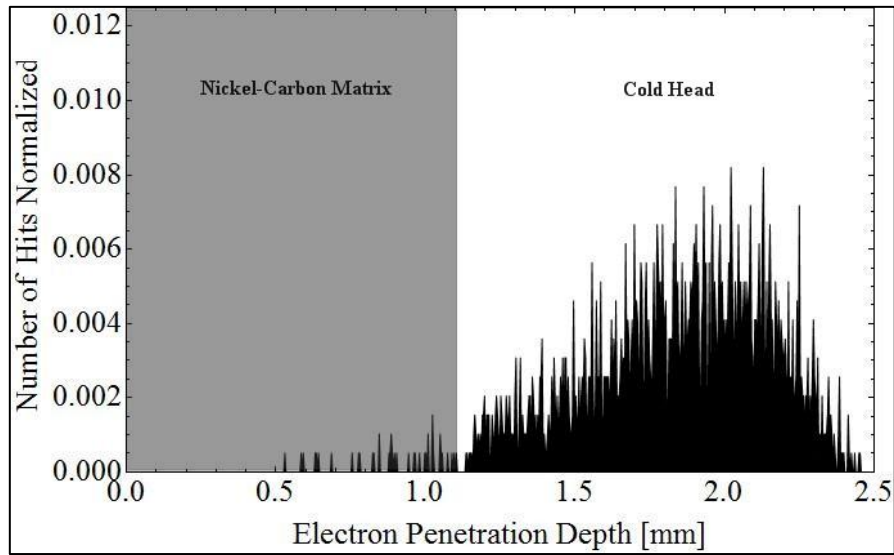


Figure 17. Results of CASINO® simulation showing electron penetration depth of 1.0 MeV electrons for a typical sample containing nickel.

The primary instrument readouts used when operating the Van de Graaff are electron energy, beam current and total coulomb count. As discussed previously the electron energy used for all irradiations was 0.5 MeV. The beam currents used were between 2 and 6 μA , and the charge count varied with desired fluence level. The beam area was fixed at 4.011 cm^2 , so the desired integrated charge could be calculated using Equation 2.

$$\text{Charge} = \text{Desired Fluence} \times \text{Charge per Electron} \times \text{Beam Area} \quad (2)$$

In Equation 2, charge is in coulombs, desired fluence is in electrons per cm^2 , and beam area is in cm^2 . However, when using the Van de Graaff, the counter does not display the total charge, but instead displays a scaled count that is some fraction of the total count. Therefore a scale correction is used to give the number of counts that should be displayed on the Van de Graaff when the desired fluence is reached. Equation 3 shows the

modified equation for determining counts needed on the Van de Graaff. For all irradiations conducted the scale was set to 6 μA , which would then be the Full Scale Factor.

$$\text{Charge} = \frac{\text{Desired Fluence} \times \text{Charge per Electron} \times \text{Beam Area}}{\text{Full Scale Factor}} \quad (3)$$

3.4.3 Irradiation Procedures

Samples were irradiated using the following procedures. First samples were mounted to the cold head by fitting them under copper wires that were attached via screws to the face of the cold head. A small strip of cellophane tape was applied to the top and bottom of the stick samples to ensure they remained fastened. Figure 18 shows two stick samples mounted to the cold head.

After the samples were secured, the cold head was bolted onto the end of the Van de Graaff beamline. Cooling water was pumped through the cold head to dissipate heat from the samples. The beamline was then evacuated to 10^{-6} Torr. Once the desired vacuum was attained, the samples were irradiated with 0.5 MeV electrons to the desired count. Samples were then removed from the Van de Graaff for post-irradiation resistivity measurements.

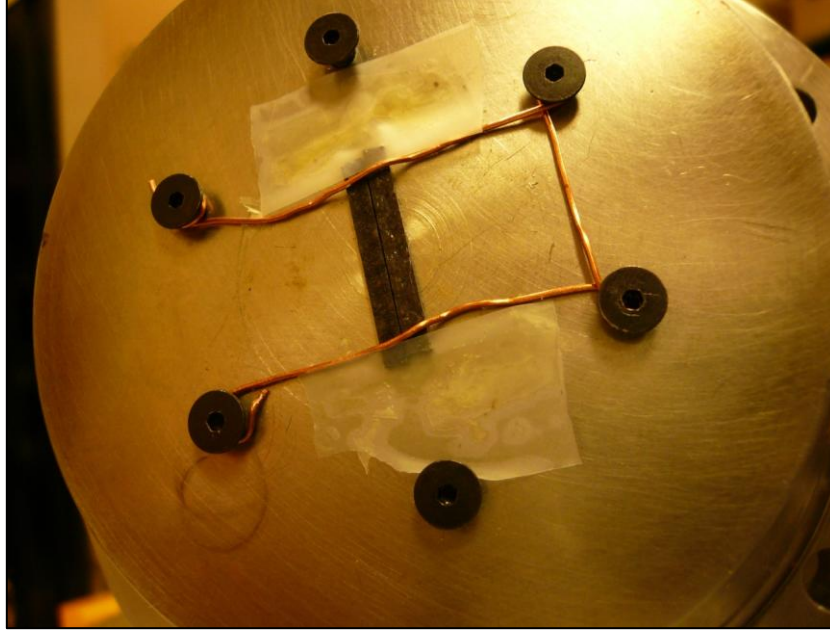


Figure 18. Two sample sticks mounted on cold head for Van de Graaff irradiations. Copper wires and cellophane tape hold the sticks in place.

3.4.4 Control Samples

Control samples were maintained for all sample types that were irradiated. Control samples were not irradiated and were re-measured with corresponding irradiated samples. In order to determine if any observed changes in resistivity could be attributed to off-gassing while under vacuum, a vacuum check was conducted. For the vacuum check, control samples were attached to the cold head and mounted on the Van de Graaff beamline. The samples were exposed to the same vacuum, 10^{-6} Torr for approximately 3 hours, then removed and re-measured.

3.5 XAFS Measurements

3.5.1 XAFS Overview

XAFS refers to the variation in photon absorption by a particular atom at photon energies close to the binding energy of a core electron bound to that atom. At low photon energies the photo electric effect dominates photon absorption, commonly characterized as the absorption coefficient, which generally decreases with increasing photon energy. For clarification, what one considers low energy varies depending on the material in

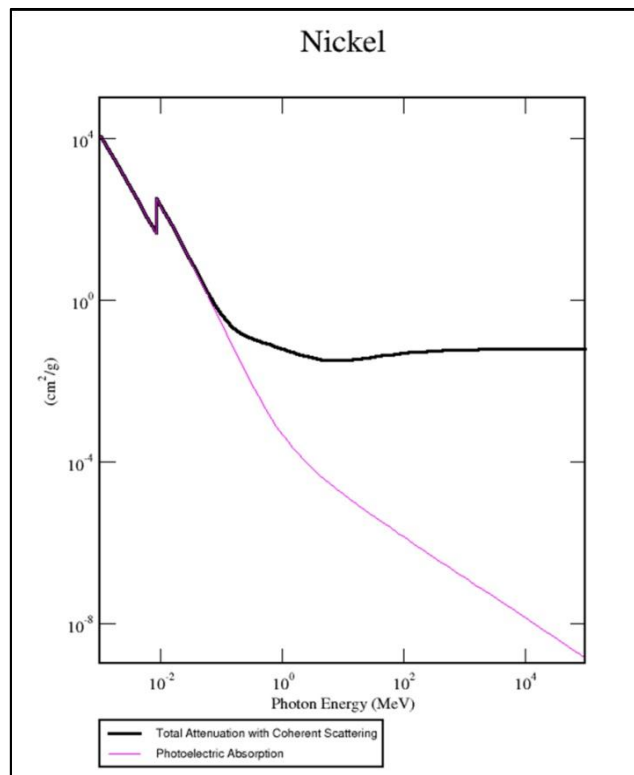


Figure 19. Photon absorption coefficient for nickel as a function of photon energy. The step just below 10^{-2} MeV corresponds to the binding energy of K level electrons in nickel.

question, but would be less than about 10 keV for nickel. A plot of absorption as a function of photon energy is shown in Figure 19. As can be seen in the graph, the

absorption exhibits a step at 8333 eV. That increase is due to the photon energy closely matching the binding energy of a K level electron in nickel. At slightly lower energies, the photon is less likely to be absorbed as there few available states for the core electron to transition to, were it to accept the photon's energy.

As photon energy increases to the electron binding energy, the photon can impart enough energy to free the electron from the atom to the continuum where the number of possible energy states is nearly limitless. As photon energy continues to increase, the probability for interaction decreases further. Such a situation is depicted in Figure 20(a). However, when the absorption is examined more closely, the presence of neighboring atoms impacts the absorption probability.

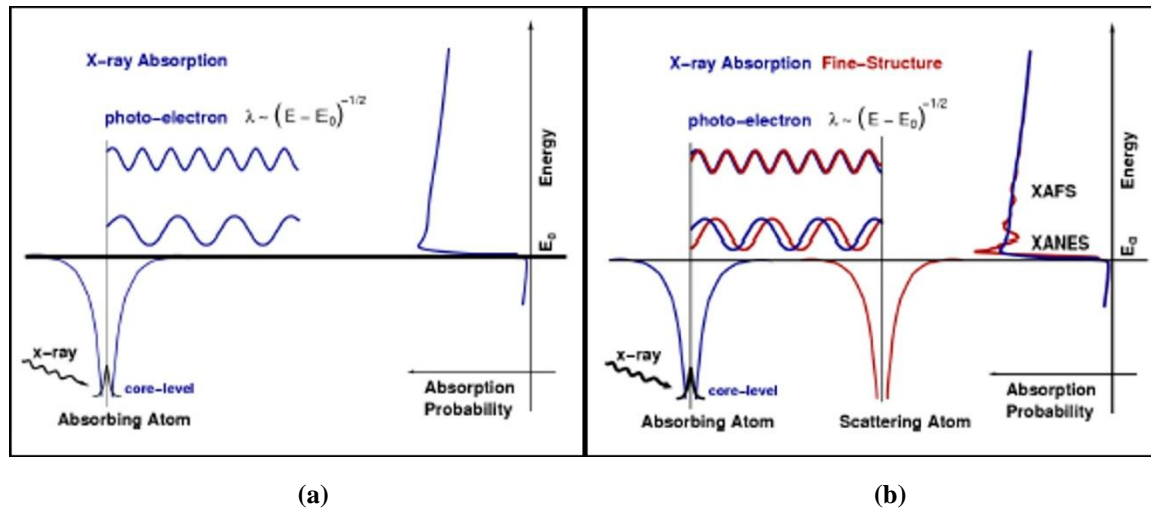


Figure 20. X-ray absorption for an isolated atom (a) and an atom with neighbors (b). For the atom in (a), the absorption coefficient decreases smoothly with increased energy beyond the absorption edge of a core electron. For the atom in (b), the wave function of the ejected electron backscatters off a neighbor atom and interferes with itself, modifying the absorption probability [22].

The right half of Figure 20 shows the effect of a neighboring atom. The wave function of the photo-electron is reflected back toward the absorbing atom where it interferes with itself positively or negatively depending on its phase. The phase in turn depends on the distance traveled and the wavelength of the photo-electron wave function. The photo-electron wavelength is dependent on the kinetic energy imparted to the photo-electron and is essentially the excess photon energy above the electron binding energy. XAFS measurements take advantage of the difference between the expected absorption spectrum for an isolated atom and the observed absorption spectrum acquired for a given sample to determine such parameters as distance to neighboring atoms and number of neighbors. This is done through application of the XAFS equation, presented as Equation 4.

$$X(k) = \sum_j \frac{N_j f_j(k) e^{-2k^2 \sigma_j^2}}{k R_j^2} \sin[2kR_j + \delta_j(k)] \quad (4)$$

In Equation 4, $f(k)$ and $\delta(k)$ are scattering amplitude and phase shift as functions of wave number, N is the number of neighboring atoms, R is the distance to the neighboring atom, σ^2 is the disorder in the neighbor distance, and j is the shell or group of atoms at approximately the same distance (within about 0.05 Å) [22].

XAFS is a powerful technique but requires specialized equipment. XAFS does not depend on a regular crystal structure, therefore amorphous materials can be investigated, and researchers from a wide variety of fields have employed XAFS, from semiconductor developers to geologists and biologists. Neither does XAFS require arduous sample preparations, as solids, liquids, and gasses can be used. The key

requirement is that of a very precisely controlled intense source of polarized X-rays, such as are produced in a synchrotron. Therefore the XAFS measurements conducted for this study were performed at Louisiana State University's (LSU) Center for Advanced Microstructure Devices (CAMD) synchrotron facility.

For XAFS measurements, two measurement modes can be employed, transmission or fluorescence, depending on the sample type. Transmission mode is the simplest and works best for thin samples that do not attenuate the x-rays below a usable signal. Fluorescence mode is used for relatively thick samples, preferably containing a low density of the target element to reduce self absorption effects. For both modes the

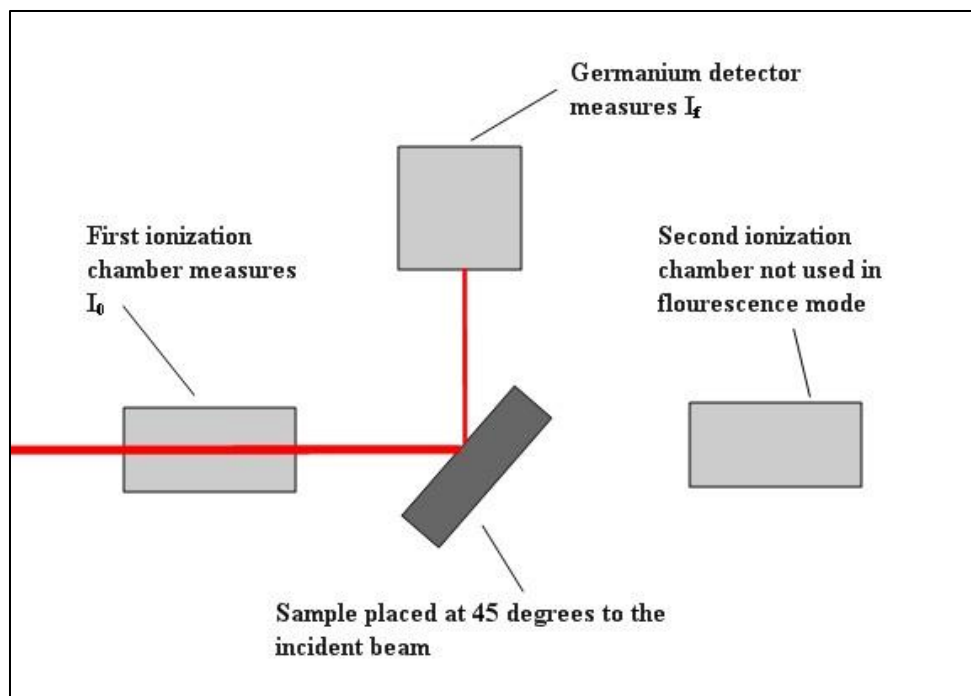


Figure 21. Schematic of XAFS setup for measurements in transmission mode. The beam travels from left to right, passing through the first ionization chamber where I_0 is measured, then through the sample where the beam intensity is attenuated, and finally through the second ionization chamber where I is measured.

incident photon beam is measured just prior to reaching the sample and again after it exits the sample via transmission or fluorescence. Figures 21 and 22 show the setup used for transmission and fluorescence measurements at the CAMD facility.

For transmission mode, the absorption coefficient is found directly from Equation 5.

$$I = I_0 e^{-\mu x} \quad (5)$$

In Equation 5, I is the measured transmitted intensity, I_0 is the incident beam intensity, μ is the absorption coefficient and x is the distance traveled through the sample. Implicit in Equation 5 are the assumptions that attenuation by other processes such as Compton Scattering and Pair production are very small compared to photoelectric absorption and that beam attenuation is negligible as it passes through the air between the first ionization chamber and the second ionization chamber. Both are reasonable assumptions for the X-ray energies used.

For fluorescence measurements, the absorption coefficient is found from Equation 6, where ϵ is the fluorescence efficiency, $\Delta\Omega$ is the solid angle of the detector, E_f is the energy of the fluorescence x-ray, θ is the incident angle of the beam relative to the sample surface, φ is the angle of the fluorescence x-rays departing the sample surface, $\mu_x(E)$ is the absorption from the target element, and $\mu_{tot}(E)$ is the total absorption in the sample, i.e. $\mu_{tot}(E) = \mu_x(E) + \mu_{other}(E)$.

$$I_f = I_0 \frac{\epsilon \Delta\Omega \mu_x(E) \left\{ 1 - e^{-\left[\frac{\mu_{tot}(E)}{\sin\theta} + \frac{\mu_{tot}(E_f)}{\sin\varphi} \right] t} \right\}}{4\pi \frac{\mu_{tot}(E)}{\sin\theta} + \frac{\mu_{tot}(E_f)}{\sin\varphi}} \quad (6)$$

For thick dilute samples, $\mu t \gg 1$ and $\mu_x \ll \mu_{\text{other}}$, then Equation 6 simplifies to Equation 7 with a Taylor series expansion of the exponential [22].

$$I_f = I_0 \frac{\epsilon \Delta \Omega}{4\pi} \frac{\mu_x(E)}{\frac{\mu_{\text{tot}}(E)}{\sin\theta} + \frac{\mu_{\text{tot}}(E_f)}{\sin\phi}} \quad (7)$$

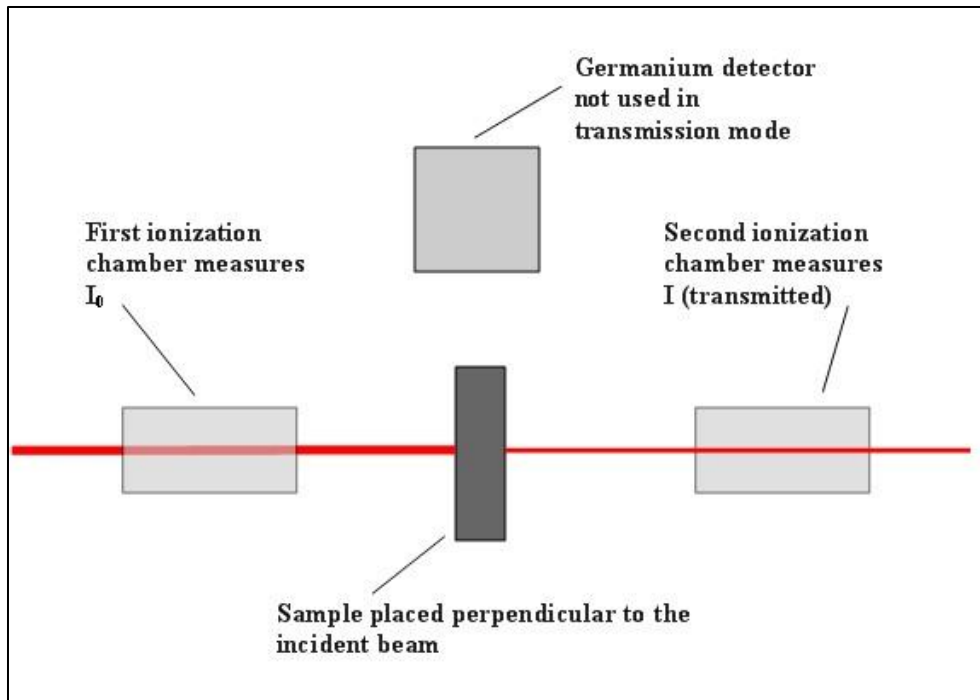


Figure 22. Schematic of XAFS setup for measurements in fluorescence mode. The beam travels from left to right, passing through the first ionization chamber where I_0 is measured, then into the sample where X-rays are absorbed, then emitted as core electron vacancies are re-filled. The fluorescence signal is measured by a 13 element germanium detector placed 90 degrees from the incident beam.

3.5.2 Measurement Setup

The XAFS measurements were conducted in the fluorescence mode with a setup as shown in Figure 22. A schematic of CAMD's Double Crystal Monochromator (DCM) beamline is shown in Figure 23. For all XAFS scans, the DCM was equipped with

germanium 220 crystals. The monochromator was tuned to 9333 eV so that incident beam intensity would increase slightly as higher photon energies were scanned, therefore improving the signal by partially compensating for the effects of lower fluorescence with higher energy. Tuning to 9333 eV also reduced the impact of higher harmonics on the scan. In Figure 23, the area labeled Experimental Hutch contained the detectors and sample that are depicted in Figure 22. The incident beam intensity I_0 was measured with a free-air ionization detector and the fluorescence signal I_f was measured using a Canberra 13 element high-purity germanium detector. Fluorescence mode was selected because the sample was thick and dilute in terms of the target element, nickel. To characterize thickness, the concept of skin depth was applied, where one skin depth is the depth into a material at which the photon beam intensity would be reduced by an exponential factor of e^{-1} .

To calculate skin depth, the power in the exponential term of Equation 5 is set to one as shown in Equation 8. Energy dependent values for the absorption coefficient μ can be found at the National Institute of Standards and Technology (NIST) database and are normally given in units of cm^2 per gram. Assuming a uniform density of nickel in a typical sample, 242 gsm gives a volume density of 0.186 g/cm^3 . The photoelectric absorption coefficient for nickel is $328 \text{ cm}^2/\text{g}$ at 8333 eV [23]. Applying Equation 8 gives a skin depth of $164 \mu\text{m}$, which is much less than the typical sample thickness of $1100 \mu\text{m}$.

$$\text{Skin Depth} = \frac{1}{\mu} \quad (8)$$

A similar calculation for carbon at the nominal sample density of 1.35 g/cm^3 yields a skin depth of $66\,000 \text{ }\mu\text{m}$, which is much greater than the sample thickness, therefore the skin depth is well approximated by the skin depth in 0.186 g/cm^3 nickel.

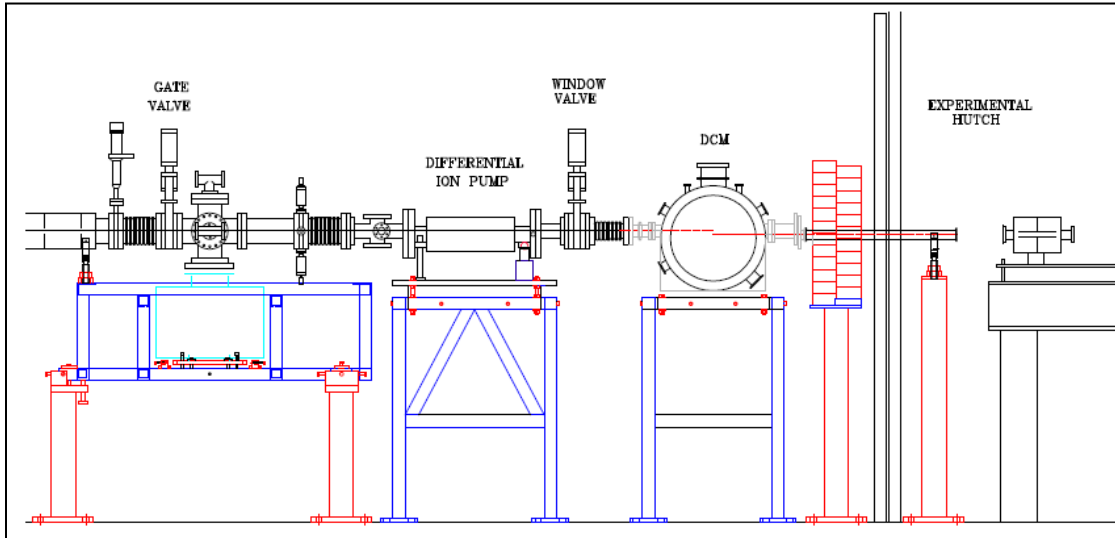


Figure 23. Sketch of the CAMD DCM beamline. X-rays exit the synchrotron and traverse the beamline from left to right. The double crystal monochromator, labeled DCM, is used to select X-ray energies used in the scan.

3.5.3 Measurement Procedures

The samples were mounted in the experimental hutch and scans were conducted by stepping the photon energy from 150 eV below the absorption edge to 947 eV above the absorption edge. Each sample was scanned at least three times, as the complexity of the material was expected to impact the quality of the signal. Beam alignment was checked repeatedly throughout the testing by placing x-ray photo paper in front of the sample and conducting a burn.

3.5.4 Measurement Results

Figure 24 shows an example of the raw data obtained from a typical XAFS measurement, in this case scan number 7 of sample Ni-36-4.

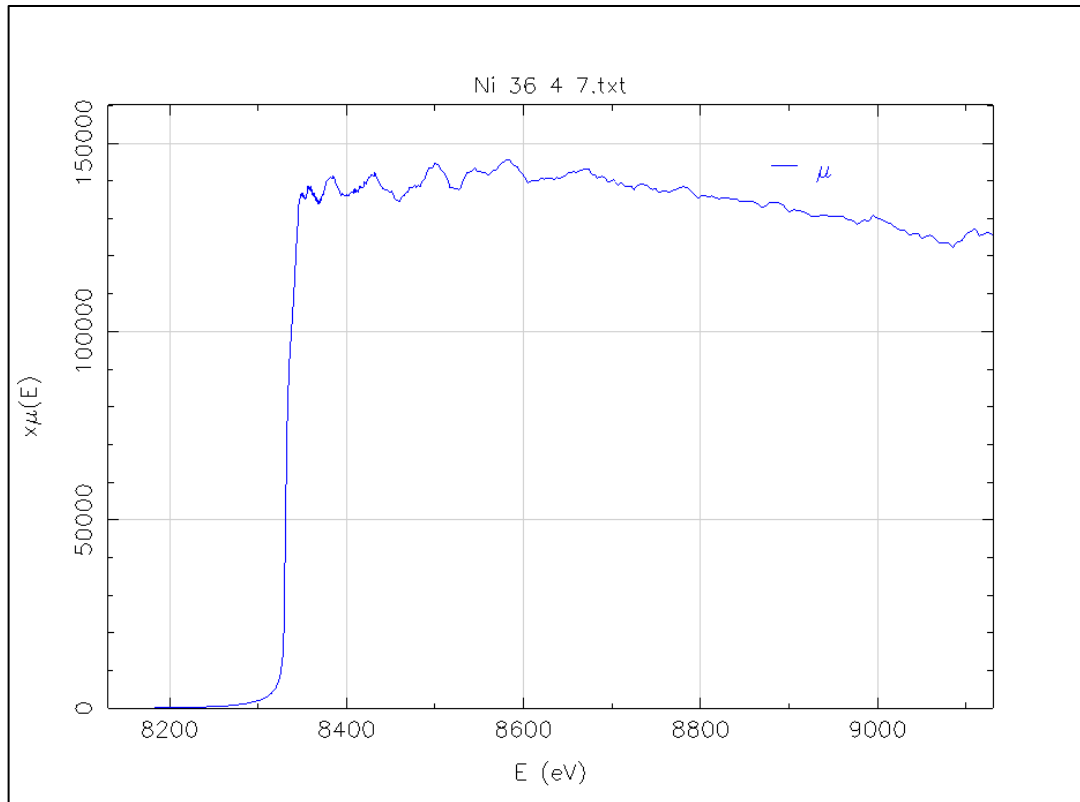


Figure 24. Absorption spectrum from a typical XAFS measurement, showing the absorption coefficient (dimensionless) as a function of photon energy.

3.6 Experimental Summary

Measurements related to electrical properties of the nickel-carbon nanocomposite samples were taken to gather pre-irradiation and post-irradiation data useful for evaluating material response. Surface resistivity measurements were taken and found to vary by amounts comparable to the possible changes for lower irradiation levels;

therefore additional measurements were taken to enable the use of statistical analysis. Bulk resistivity measurements were obtained and found to be inadequate for discriminating changes at the levels observed. Electron beam irradiations were conducted at the WSU Van de Graaff facility using 0.5 MeV electrons. Finally, post irradiation surface resistivity and XAFS measurements were obtained.

IV. Results and Analysis

4.1 Overview

Results from surface resistivity and XAFS measurements showed no increased surface resistivity and no oxide formation following irradiation. The observed changes in surface resistivity were much smaller than previously reported and none of the samples increased in resistivity as indicated in [4]. For all sample types, measurements showed a decrease of between 14% and 30% in surface resistivity following irradiation to a total electron fluence of $4 \times 10^{16} \text{ cm}^{-2}$. XAFS measurements indicated a decrease in NiO content for two sample types, Ni-36 and sample type C used in [4]. Bulk resistivity measurements were not used for evaluating material response due to the wide variation in measurements obtained from the same sample. From the data, no discrimination could be made between epoxy type and material response, and the expected dependence on sample orientation with respect to electron beam direction was not observed.

4.2 Surface Resistivity Analysis

Surface resistivity results were analyzed in terms of the relative change in resistance measured for each sample, and results showed a decrease in resistivity following irradiation for some measurements and no measurable change for others. Because resistance is related to resistivity by sample geometry, as shown in Equation 9, and because the sample and measurement geometry did not change throughout the experiment the relative change in resistivity is equal to the relative change in resistance.

$$\rho = \frac{wt}{s} \frac{V}{I} \quad (9)$$

In Equation 9, ρ is resistivity, V is voltage, I is current, w and t are sample width and thickness, and s is probe spacing used in the four point setup [24].

Table 4 shows the results of pre- and post-irradiation measurements for four sample types that were irradiated to $2 \times 10^{16} \text{ cm}^{-2}$. The pre-irradiation averages in Table 4, column 3, were calculated from three measurements of each sample, with the exception of sample C-3-5, which was calculated from 20 measurements. As was discussed earlier, post-irradiation measurements showed much smaller changes than the 77 to 440% reported previously, and therefore the precision of the measurements was not adequate to determine the relative change. The follow-on measurements, taken in sets of 20 each were used to develop distributions and 68% confidence intervals.

Table 4. Comparison of pre-irradiation and post-irradiation resistivity measurements for samples irradiated to $2 \times 10^{16} \text{ cm}^{-2}$. Relative change was estimated by taking the difference between the pre-irradiation average and the post-irradiation average. Note C-3-5 pre-irradiation values were measured as a large distribution and therefore the 68% confidence interval was used for the minimum and maximum values.

Pre-Irradiation Measurements					Post Irradiation $2 \times 10^{16} \text{ cm}^{-2}$			
Sample	Dot Alignment	Average Measured Resistance [m Ω]	Minimum [m Ω]	Maximum [m Ω]	Average Measured Resistance [m Ω]	68% Interval		Relative Change in Mean Value [%]
						68% Interval Lower Limit	68% Interval Upper Limit	
Ni-36-1	up	135.5	132.7	139.7	129.0	124.9	136.4	-4.8
Ni-36-1	down	155.7	150.2	159.4	154.2	149.8	160.1	-1.0
C-36-2	up	184.4	180.7	186.5	153.7	152.8	154.5	-16.6
C-36-2	down	168.7	166.2	170.1	142.2	140.3	144.6	-15.7
C-3-5	up	160.0	156.2	165.8	149.1	145.9	154.2	-6.8
C-3-5	down	157.0	147.0	165.9	138.4	125.8	149.6	-11.8
Ni-3-1	up	195.3	191.7	197.4	168.0	164.9	170.8	-14.0
Ni-3-1	down	181.7	180.8	182.5	162.3	158.2	166.3	-10.7

To investigate possible radiation effects, the three pre-irradiation measurements and their average was compared to the mean and the 68% confidence interval of the larger, post-irradiation set. In the case of sample Ni-36-1, two of the three measurements from the smaller three measurement set, as well as the average value, were found to be within the 68% confidence interval of the larger 20 measurement post-irradiation set and thus, it cannot be said that a measurable change occurred. The same result was found for both sides of the sample. For samples C-36-2 and Ni-3-1 in Table 4, all values from the smaller measurement sets were found to be outside the confidence intervals of the larger sets, and thus the differences are more likely to represent a real change in resistivity. In the case of sample C-3-5, the 68% confidence intervals for dot up configuration did not overlap, and the 68% confidence intervals for dot down configuration overlapped only slightly, thus indicating that a real change in resistivity was likely measured.

Table 5 shows the results of pre- and post-irradiation measurements for sample types that were irradiated to $4 \times 10^{16} \text{ cm}^{-2}$. Again, the pre-irradiation averages were calculated from three measurements of each sample, with the exception of sample C-3-3, which was calculated from 20 measurements. At this larger fluence, all samples showed clear decreases in resistivity in direct contrast to the previous results, indicating that oxide formation at the surface did not govern the changes to surface resistivity following irradiation. A final note on Tables 4 and 5 is that the numbers in bold indicate measurements of the sides that were facing away from the electron beam during irradiations. In all cases but one, the side facing away from the beam showed less change in resistivity than the side facing towards the beam. This result was unexpected, as it was

believed the greater energy deposition in the far side would lead to a greater change in resistivity.

Table 5 Comparison of pre-irradiation and post-irradiation resistivity measurements for samples irradiated to $4 \times 10^{16} \text{ cm}^{-2}$. Relative change was estimated by taking the difference between the pre-irradiation average and the post-irradiation average. Note C-3-3 pre-irradiation values were measured as a large distribution and therefore the 68% confidence interval was used for the minimum and maximum values

Pre-Irradiation Measurements					Post Irradiation $4 \times 10^{16} \text{ cm}^{-2}$			
Sample	Dot Alignment	Average Measured Resistance [m Ω]	Minimum Value [m Ω]	Maximum Value [m Ω]	Average Measured Resistance [m Ω]	68% Interval		Relative Change in Mean Value [%]
						68% Interval Lower Limit [m Ω]	68% Interval Upper Limit	
Ni-36-1	up	135.5	132.7	139.7	102.4	100.1	104.1	-24.4
Ni-36-1	down	155.7	150.2	159.4	132.6	120.4	148.4	-14.8
Ni-36-6	up	144.0	138.6	148.1	121.1	118.9	124.2	-15.9
Ni-36-6	down	160.1	158.7	161.2	112.8	109.2	118.2	-29.5
C-36-2	up	184.4	180.7	186.5	131.8	131.0	132.6	-28.5
C-36-2	down	168.7	166.2	170.1	125.2	124.1	126.5	-25.8
C-3-3	up	284.0	261.7	315.6	203.4	190.0	220.1	-28.4
C-3-3	down	197.2	195.9	198.3	164.5	162.0	169.6	-16.6
Ni-3-1	up	195.3	191.7	197.4	155.5	148.9	159.1	-20.4
Ni-3-1	down	181.7	180.8	182.5	155.7	153.8	157.7	-14.3

The plots in Figures 25 through 28 depict the changes in surface resistance for one sample of each material type. The uncertainty associated with each marker is $\pm 0.1 \text{ m}\Omega$ which is less than the marker size, therefore error bars have not been included in the plots. The plots show the general decreases with fluence discussed previously while highlighting the variability in the measurements. Note that sample C-3-3 did not include an intermediate measurement at $2 \times 10^{16} \text{ cm}^{-2}$.

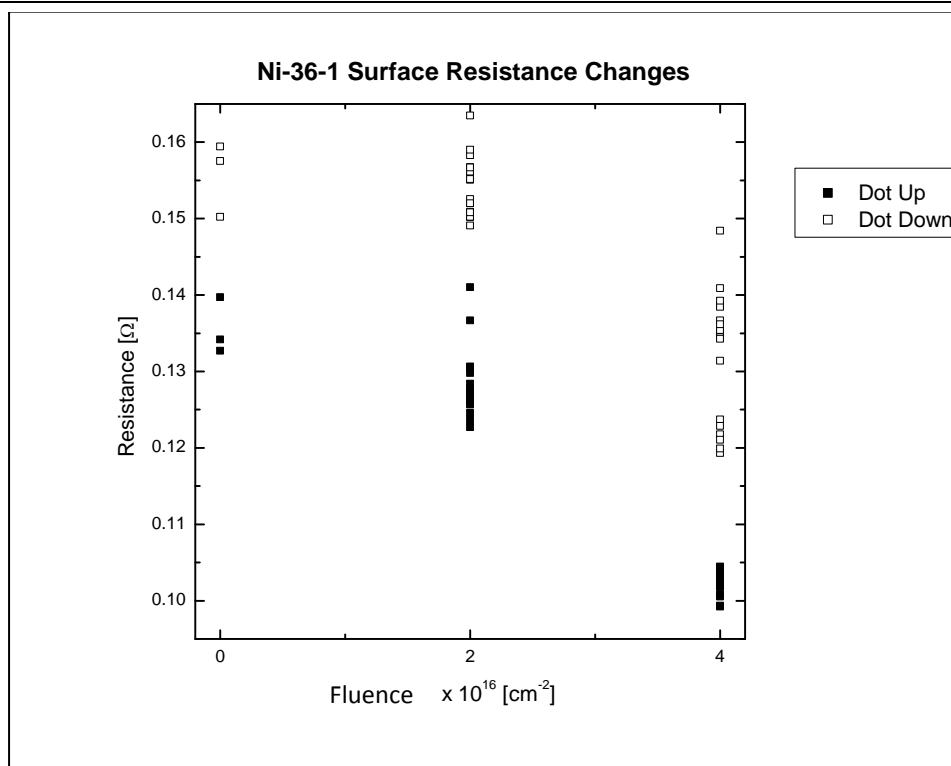


Figure 25. Surface resistance as a function of fluence for sample Ni-36-1.

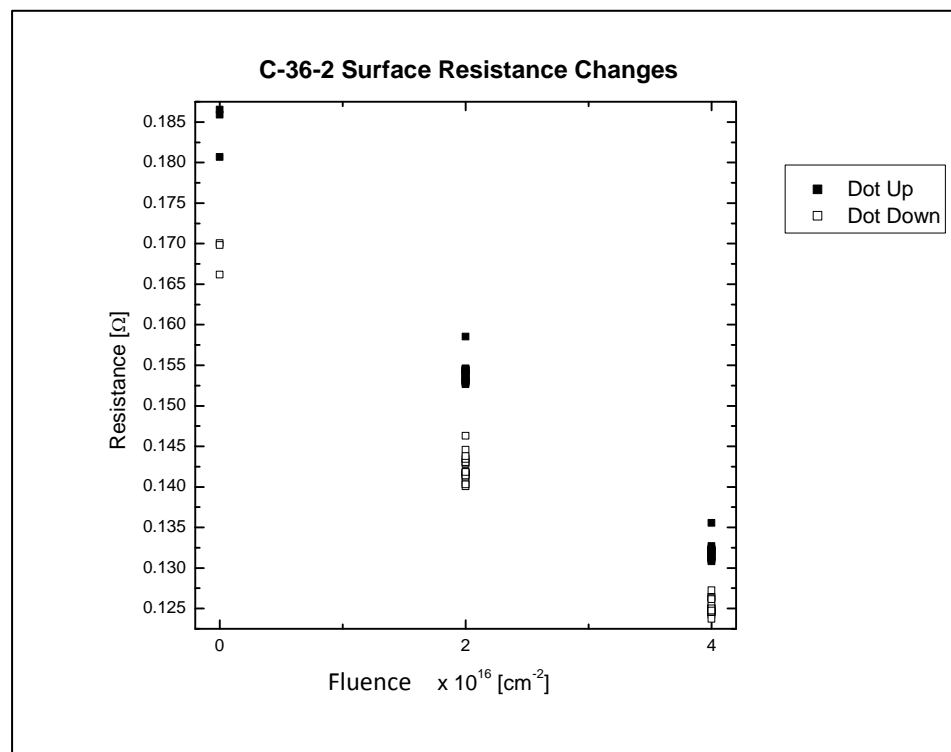


Figure 26. Surface resistance as a function of fluence for sample C-36-2.

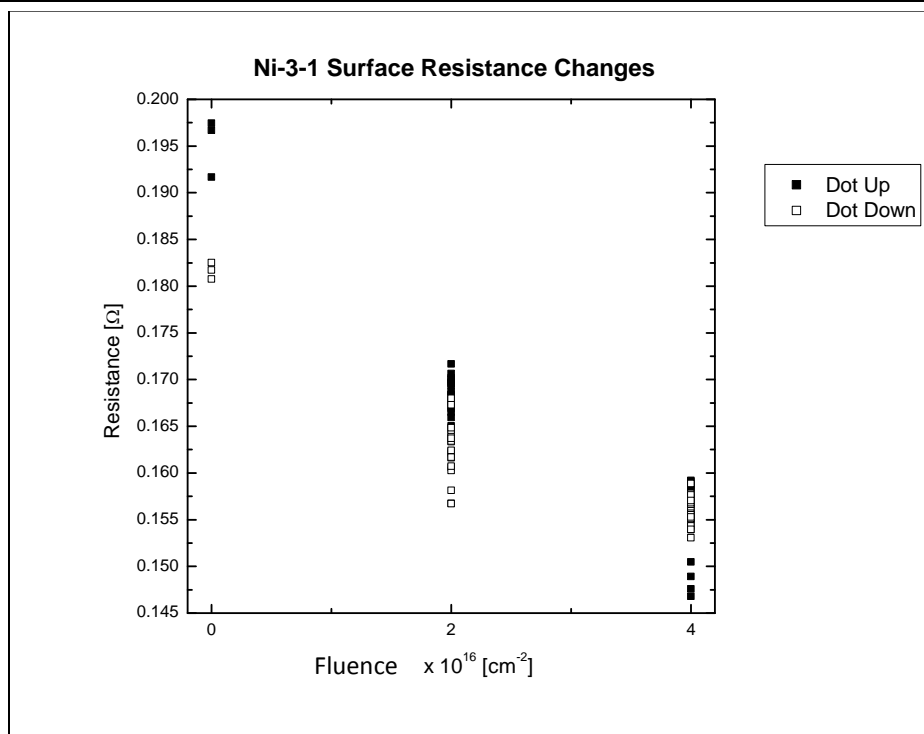


Figure 27. Surface resistance as a function of fluence for sample Ni-3-1.

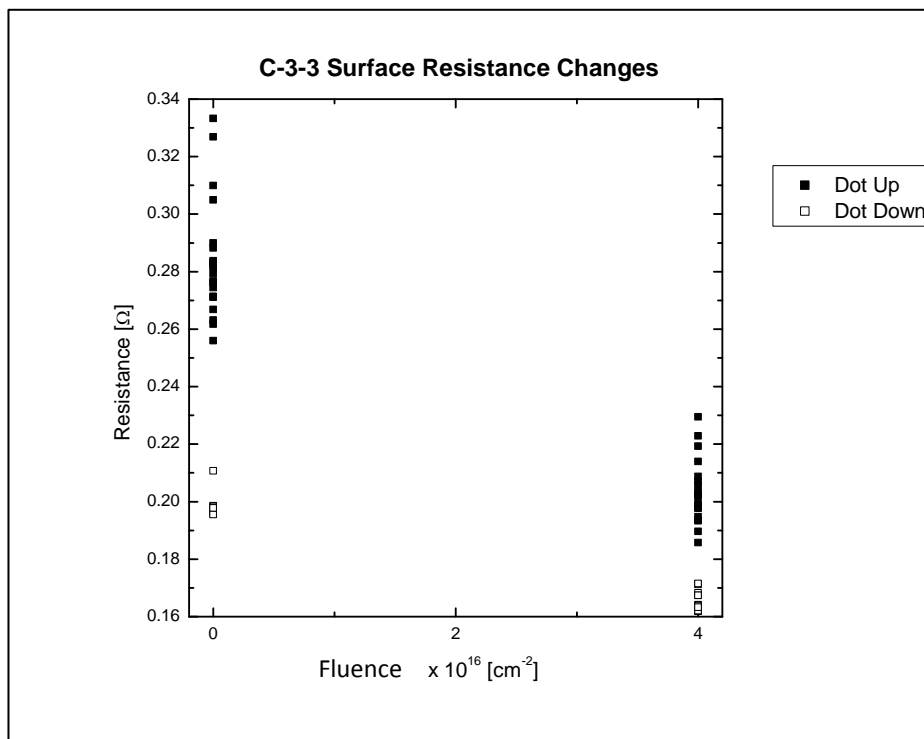


Figure 28. Surface resistance as a function of fluence for sample C-3-3.

The surface resistivity variation was not Gaussian, based on a statistical analysis of the larger data sets. Best fits for distributions and P-tests were conducted on each of the sample types. Although some samples passed P-tests for Gaussian distributions, only one showed a good match for the Gaussian distribution and all matched other distributions much more closely. A typical example is shown for sample Ni-36-1 in Figure 29. The results of a P-test indicated a 23% probability that the data came from a Gaussian distribution. The standard criteria for rejecting the Gaussian distribution is a P value below 0.05, then it could be stated with a 95% confidence the data is not from a Gaussian distribution [25].

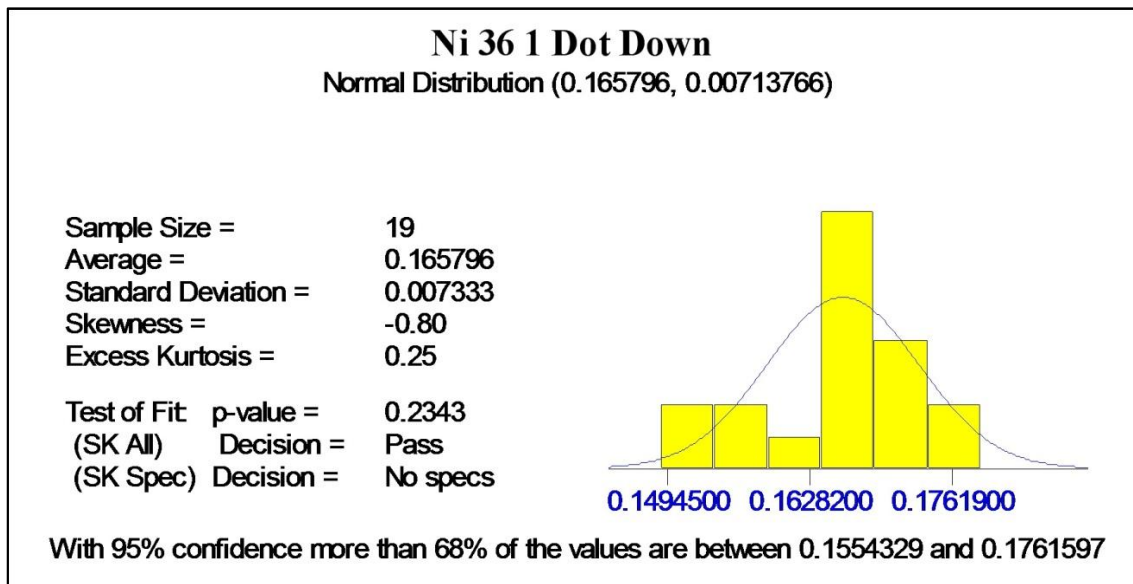


Figure 29. Comparison of sample measurements to the Gaussian distribution for sample Ni-36-1 in the dot down orientation. The P-value of 0.2343 indicates a 23% probability the data came from the Gaussian distribution

It is interesting to note that while Figure 29 shows that the sample measurements passed the P-test for a Gaussian distribution, measurements of the opposite side of the same sample, taken in the dot up orientation failed the P-test for a Gaussian distribution, as shown in Figure 30.

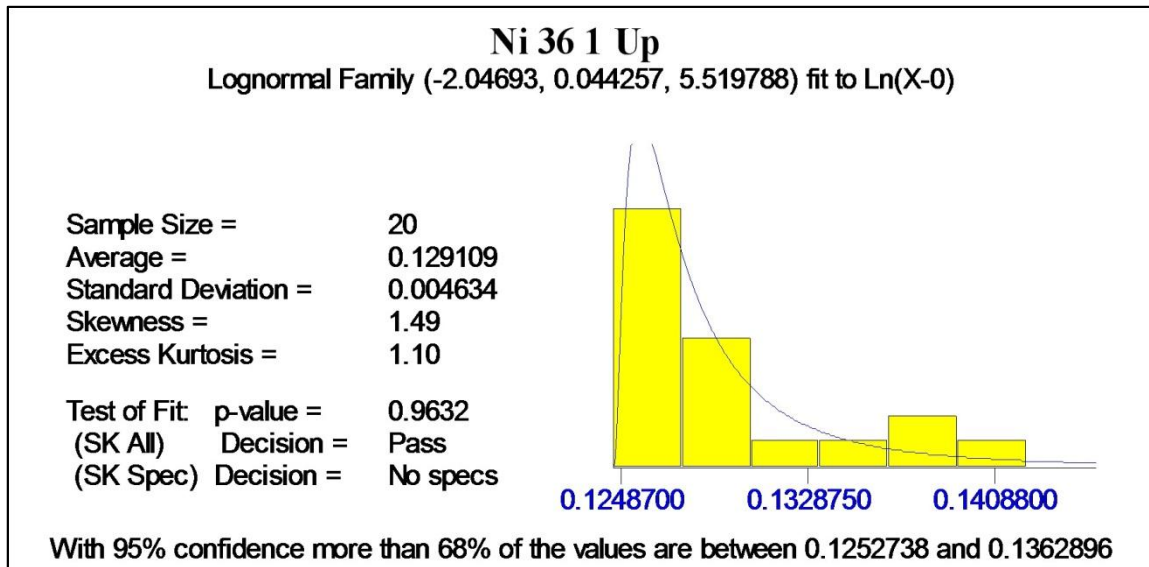


Figure 30. Comparison of sample measurements to the Gaussian distribution for sample Ni-36-1 in the dot up orientation. The P-value of 0.0243 indicates a 2.4% probability the data came from the Gaussian distribution, thus the Gaussian distribution is rejected.

Table 6 shows the results of P-tests for Gaussian and best fit distributions for samples of each material type used. The departures from Gaussian distribution are believed to be a result of the combination of factors including systematic errors associated with the measurement method and variations in the material. The surface resistance measurement is designed for homogeneous materials with smooth surfaces. Such materials would contact the probes in a consistent manner each time they were placed in the sample holder. Moreover, small changes to the position of samples in the

holder should not produce significant changes in the measurements, as the current paths and induced electric fields would have much smaller variations for a uniform material. In effect, the current injected at probe 1 would experience the same conditions even if the position of probe 1 was moved slightly towards the center or towards the nearest edge of the sample. In contrast, the irregular surface roughness of composite materials would be expected to change both the surface area contacting the probes and the path along which current flows between the probes. Variations in the composite, ie. higher or lower nickel concentration, variations in surface roughness, and variations in separation between the woven carbon sheets, could change the electric field penetration depths and result in different conduction paths for the current through the material.

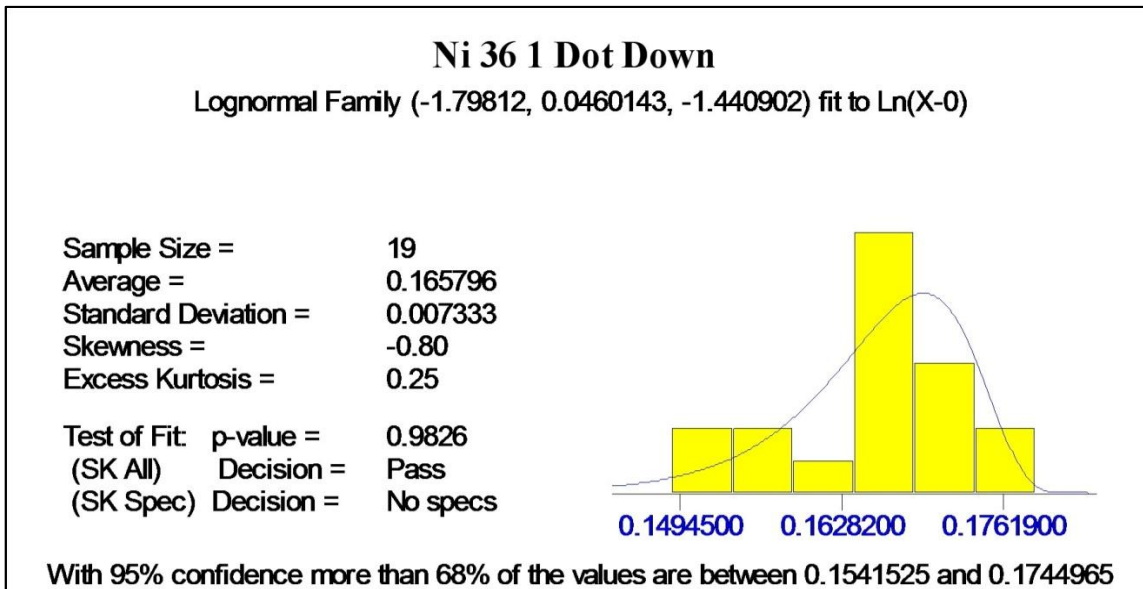


Figure 31. Best fit distribution for surface resistivity measurements of sample Ni 36 1 taken in dot down orientation. The P-value of 0.9826 shows a 98% probability the data matches the distribution.

Table 6. P-test results of Gaussian fit for measurements taken of each sample type used.

Sample Designation	Dot Orientation	Gaussian Pass/Fail	P-test Value	Best Fit Distribution	P-test Value
Ni-36-1	Up	Fail	0.0243	Lognormal	0.9632
Ni-36-1	Down	Pass	0.2343	Lognormal	0.9826
C-36-2	Up	Fail	0.0486	Johnson	0.9096
C-36-2	Down	Pass	0.1274	Johnson	0.9820
Ni-3-1	Up	Pass	0.7729	Johnson	0.9888
Ni-3-1	Down	Pass	0.8348	Loglogistic	0.9751
C-3-3	Up	Pass	0.0582	Pearson	0.9579
C-3-3	Down	Pass	0.4933	Johnson	0.9445

Two of the additional measurements were examined to estimate the effects of imprecise sample placement and surface roughness. Those two measurements consisted of the graphite only sample and sample Ni-3-1 measured with the alternate setup, i.e. contacting the post. For the measurements taken with sample Ni-3-1 contacting the post, the 68% confidence interval was 1.9% of the measurement average as compared to 3.6% for measurements taken with the sample placed in the center of the holder. It is also worth noting that the magnitude of the resistance was 156 mΩ when contacting the post, compared to 168 mΩ for the same sample when not contacting the post. This may be due to an alternate ground path as mentioned in the experiment section. For the measurements taken with the graphite stick, the 68% confidence window was 1.4% of the measurement average, which is lower than 14 of the 16 measurement distributions, as in

Table 7. The only comparable measurement was sample C-36-2 in the dot up orientation, which showed a very small variation. These two additional measurement configurations showed that variation in the placement of the sample within the holder could account for half of the measurement uncertainty for some of the samples used and that the surface roughness contribution to measurement variation could be between 0 and 17%, depending on the sample.

Figure 32 shows the difference in surface roughness between two samples. The top image shows a profile view of sample Ni-36-1, which had the largest variation in measured surface resistance. The bottom image shows a profile view of sample C-36-2, which had the smallest variation in measured surface resistance. Both samples have irregular surface features, but the magnitudes of those features are less in sample C-36-2, which corresponds to the lower variability in surface resistance measurements. Moreover, the top surface of sample Ni-36-1, as it appears in Figure 32, showed a greater variation in measurements than the bottom, less rough surface. It also appears that sample Ni-36-1 has some voids within the sample bulk that would further contribute to variations in measurements depending on probe placement, as both the applied electric fields and the current paths would be impacted by the void locations. Additional research would be required to accurately establish the contributions from the combined effects of surface roughness, bulk voids, and sample placement.

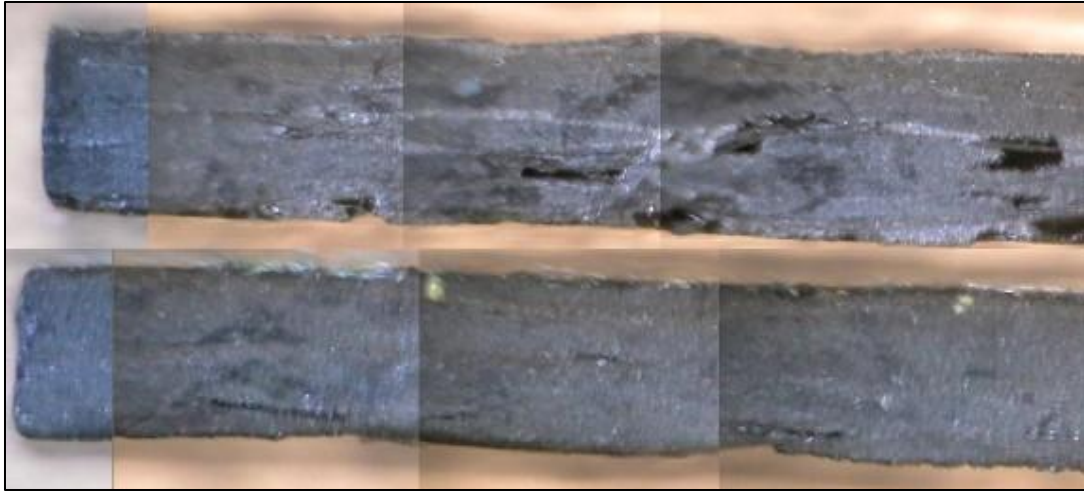


Figure 32. Profile views of samples Ni-36-1 (top) photographed with dot down, and C-36-2(bottom) photographed with dot up. The thickness (vertical in picture) of both samples is approximately 1 mm. Note the relative rougher surface of Ni-36-1, and the voids within its bulk.

Although the results of surface resistivity measurements did not agree with previous results from a similar investigation conducted at AFIT [4], the outcome was not entirely unexpected. The decrease in resistivity for carbon composites seems reasonable if the most dielectric of the components, the epoxy, decreased in resistivity following irradiation. Such a result would be consistent with the studies conducted by Sisman and Bopp at ORNL that showed a decrease in volume resistivity for polyethylene sheets following irradiation [13]. Moreover, the smaller changes measured in this research versus those reported in [4] seem reasonable when compared to the radiation tolerances given in Figure 4 from reference [17]. The fluence levels used for the current investigation were consistent with mild to moderate physical degradation, and as discussed previously, permanent changes to electrical properties are generally much smaller in polymers than changes to mechanical properties and physical degradation.

Table 7. Measurement confidence window as a percentage of measurement average for each of the samples used and the graphite sample. Note that the graphite sample was not irradiated, so both values given are for non-irradiated configurations.

Sample	Dot Orientation	68% Confidence Window [%] Following $2 \times 10^{16} \text{ cm}^{-2}$	68% Confidence Window [%] Following $4 \times 10^{16} \text{ cm}^{-2}$
Ni-36-1	up	8.5	3.9
Ni-36-1	down	12.7	21.1
C-36-2	up	1.3	1.2
C-36-2	down	3.5	1.9
Ni-3-1	up	3.6	6.6
Ni-3-1	down	4.9	2.5
C-3-3	up	19.0	14.8
C-3-3	down	2.5	4.6
Graphite	n/a	1.4	1.4

Additional insight into the energy absorption and resulting changes can be obtained with a first order calculation based on the scissioning and cross-linking rates for polyurethane presented in [15]. If it is assumed that 50% of the electron beam energy is deposited in the sample, then a fluence of $4 \times 10^{16} \text{ cm}^{-2}$ would transfer 700 J to the sample. Then applying the G(S) and G(X) values of 0.14×10^{-7} and 0.12×10^{-7} moles/J respectively, the energy deposited would be sufficient to cause scissioning in 4×10^{-6} moles and cross-linking in 5×10^{-6} moles. Assuming an average molecular weight of 10^4 g/mole [26], the average sample would contain less than 7×10^{-6} moles of polymer. Scissioning and cross-linking could then occur in approximately 5/7 and 4/7 of the polymer molecules present. The actual fractions would be smaller, as some portion of the electron beam energy would be absorbed in the layers of woven carbon fiber.

Although this research did not identify the radicals formed and cross-linking structures resulting from irradiation for the polymer binders used, references [26] and [27] provide some insight as to what potential radicals and ensuing reactions may arise in the polyurethane binder. Reference [26] examined a polyester based polyurethane binder

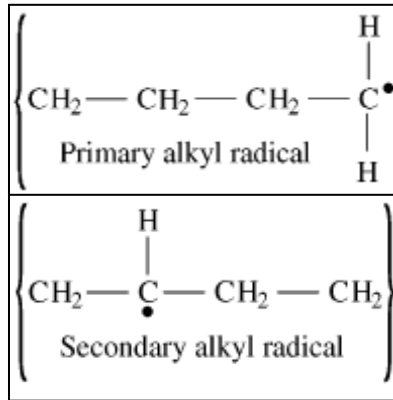


Figure 34. Primary and secondary alkyl radicals as reported in reference [26]

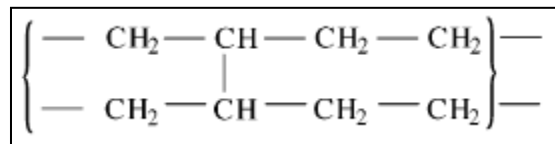


Figure 33. Cross-linking reaction found after irradiation of polyester based polyurethane binder from reference [26]. Similar reactions may take place in the polyurethane binder used for the current research.

following irradiation and found primary and secondary alkyl radicals in addition to the cross-linking shown in Figure 33. Both references [26] and [27] found results consistent with hydroperoxide formation, which can participate in many different subsequent reactions, to include decomposition resulting in the formation of alkoxy and hydroxyl radicals, both of which can contribute to the formation of additional secondary alkyl radicals discussed above and further cross-linking of the type shown in Figure 33.

Although the magnitudes of measured resistance changes were not unexpected, the fact that the sides facing away from the electron beam changed more than the incident side was unexpected. Several possible explanations have been considered, two of which were that either the energy deposition model was inaccurate or the polymer response was not simply proportional to the local energy deposition. The first explanation appears more likely as at least one previous experiment has shown energy deposition profiles match radiolytic yields in polyurethane samples for 200 keV electrons [27]. Moreover, the collisional stopping power for electrons of intermediate energies, 200 eV to 1 keV, has been shown to exhibit a strong peak for carbon [28]. For composite samples, this could provide one explanation as to why the surface resistivity measurements showed less change in the sides of the samples that were facing away from the electron beam. As electrons pass through the sample and lose energy, greater energy loss occurs within the carbon sheets per distance traveled as compared to the polymer binder. Thus a lower portion of the energy is transferred to the polymer binder. At higher electron energies, the difference in stopping power between carbon and other light elements, $Z < 10$, is much less pronounced, therefore the polymer material closer to the incident side would absorb proportionally more energy than that on the far side. If this explanation is correct, the first-order modeling of the samples was not sufficiently detailed to show such differences in the energy deposition profiles.

Another possible explanation for the different responses between the two sides is that knock-on damage is contributing more to the overall material changes on the beam side than on the far side. This possibility could be understood in terms of electron

energy. Electrons incident upon the material surface have the greatest average energy and are thus more likely to interact with the nucleus of an atom in the target material. Electron-nuclear interactions could transfer sufficient energy to knock the target atom out of its position in its crystallite lattice. As electrons pass through the material they lose energy, thus electron-nuclear interactions and the possibility for knock-on damage would be less likely on the far side of the sample.

The final area of analysis performed with regards to the surface resistivity measurements was to approximate the true surface resistivity of the samples from the measured resistance. To do so, equations 10 and 11 were employed.

$$\rho = G \frac{V}{I} \quad (10)$$

$$G = \frac{2 \pi s}{F} \quad (11)$$

Together equations 10 and 11 give the surface resistivity, ρ , for an infinitely long bar. In the equations, V is voltage and I is current as measured from the four point surface resistivity setup. G is a geometry correction factor that depends on the probe spacing, s, and the factor F, which is in turn a function of sample width, height, and length. F can be found from the graph on page 33 of reference [29], which contains the Haldor Topsoe geometric correction factors for four point resistivity measurements. Results were calculated for one of each sample type following irradiation to $2 \times 10^{16} \text{ cm}^{-2}$ and are presented in Table 8. Those values were selected because they represented the lowest irradiation level for which full distributions were calculated for most of the sample types. All of the calculated resistivity values were within the range of values calculated in [4].

Table 8. Surface resistivity calculation results obtained using the infinite bar approximation and 68% confidence windows for the best fit distributions.

Sample/ Orientation	Resistivity [$m\Omega$ -cm]	Lower Bound 68% Interval [$m\Omega$ -cm]	Upper Bound 68% Interval [$m\Omega$ -cm]
Ni-36-1 up	16.7	16.2	17.6
Ni-36-1 down	19.9	19.3	20.7
C-36-2 up	15.2	15.1	15.3
C-36-2 down	14.1	13.9	14.3
Ni-3-1 up	21.3	20.9	21.6
Ni-3-1 down	20.5	20.0	21.1
C-3-5 up	15.5	15.2	16.1
C-3-5 down	14.4	13.1	15.6
Graphite	15.5	15.3	15.7
Ext1	106	101	118

Sample EXT1 from [4] was also measured in for this investigation and was found to have a resistivity of 106 $m\Omega$ -cm versus 108 $m\Omega$ -cm reported previously. The primary discrepancy was in the uncertainty which was previously reported as 1 $m\Omega$ -cm but found here to be closer to 10 $m\Omega$ -cm. It must be emphasized that the resistivity values presented in Table 8 are only approximations and that further corrections would be required to obtain an accurate measure of the true surface resistivity.

To estimate the magnitude of such corrections necessary to attain the true resistivity, resistivity values were recalculated using the results of a finite element analysis presented in reference [24]. The results are presented in the second and third columns of Table 9. Those results are approximately half the values calculated using the infinite bar corrections and less. Lower values were expected because the approximations used in infinite bar corrections were that the material was homogeneous and that the ends of the stick were far from the measurement probes. The differences

Table 9. Surface resistivity calculations using corrections derived from finite element analysis presented by Zimney et al. compared to calculations using infinite bar approximations. The minimum and maximum true resistivity values depend on the assumed bulk resistivity through the material. The lowest value was assumed to be 1.7 [mΩ-cm] corresponding to the resistivity of the carbon fiber. The maximum resistivity value was assumed to be those found in reference [4]. The lower bulk resistivity results in a larger correction factor and thus gives the maximum true resistivity in column 3.

Sample	Min True Resistivity [mΩ-cm]	Max True Resistivity [mΩ-cm]	Infinite Bar Approximation [mΩ-cm]
Ni-36-1 up	6.11	8.26	16.7
Ni-36-1 down	7.30	9.86	19.9
C-36-2 up	2.01	7.73	15.2
C-36-2 down	1.86	7.15	14.1
Ni-3-1 up	7.68	10.4	21.3
Ni-3-1 down	7.42	10.0	20.5
C-3-5 up	2.21	8.51	15.5
C-3-5 down	2.05	7.90	14.4
Graphite	8.24	8.24	15.5
EXT1	35.7	55.7	106

between the two results highlight the complexity of conduction through the material and emphasize the fact that simple ohmic conduction does not accurately describe the current flow.

4.3 Bulk Resistivity Analysis

Due to the variation in measurements discussed earlier, bulk resistivity results were not analyzed for post irradiation changes. Further refinement of bulk measurement procedures is required before such analysis could begin. It may be prudent to depart from the IEC standards, so as to allow more flexibility in the available techniques. Whatever measurement procedure is established, of paramount importance is the need to ensure a confidence interval of less than 20% in order to detect changes in bulk resistivity following irradiations similar to those used for this research.

4.4 EXAFS Analysis

4.4.1 Summary

Results of the XAFS measurements suggested there was no significant oxide content on the sample surfaces, and that oxide content decreased for irradiated samples compared to non-irradiated samples from the same material. The XAFS results showing decreased oxide content near the surface were consistent with the decrease in resistivity shown in the surface resistivity measurements.

4.4.2 Data Processing

A qualitative analysis of the absorption spectra indicated no significant oxide content on the surface. The first step was to align and merge the several scans from each

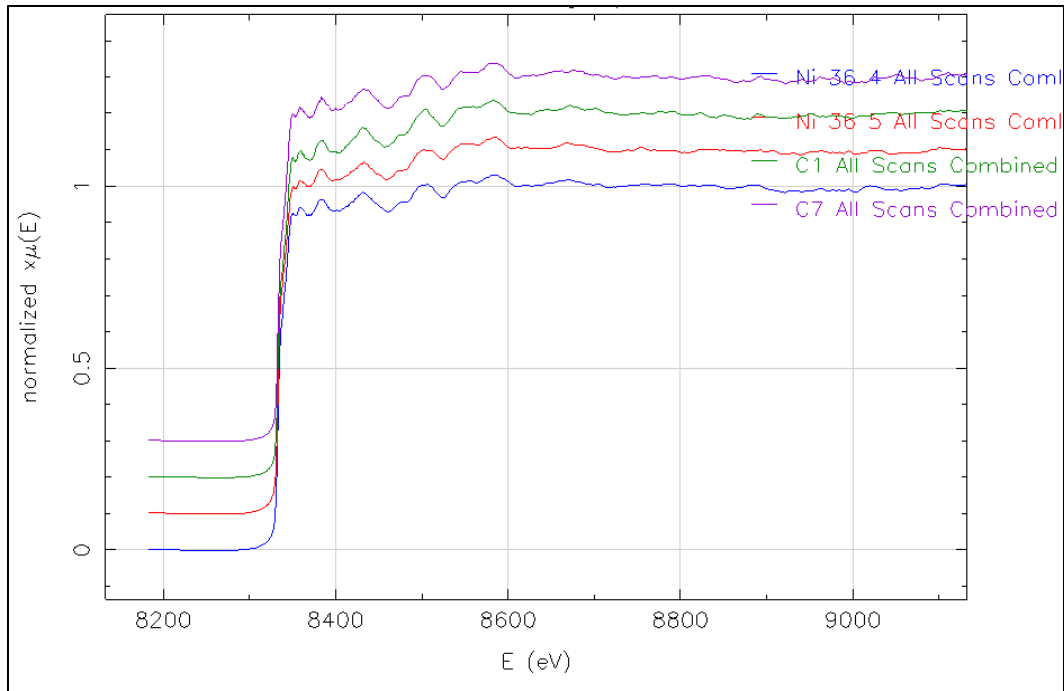


Figure 35. Absorption spectra for all the samples. From top to bottom the samples represented are Ni-36-4, C1, Ni-36-5, and C7. Samples Ni-36-4 and C1 were irradiated to $1 \times 10^{16} \text{ cm}^{-2}$, while the other two samples were not irradiated.

sample. The absorption spectra of all the samples are shown in Figure 35. The first notable feature is the similarity between the scans. This was somewhat expected due to the nature of the measurement and its ability to single out nickel atoms. Figure 36 shows the absorption spectra from samples of carbon composites with nickel nanoparticles published by Nietubyc et al. [21]. Notice the large peak that is present in the nickel-oxide spectrum but absent from the pure nickel spectrum. The other spectra, labeled 1 through 6 were obtained from samples with varying levels of NiO. The spectra from the samples used for the present investigation appear to most closely match the pure nickel spectrum.

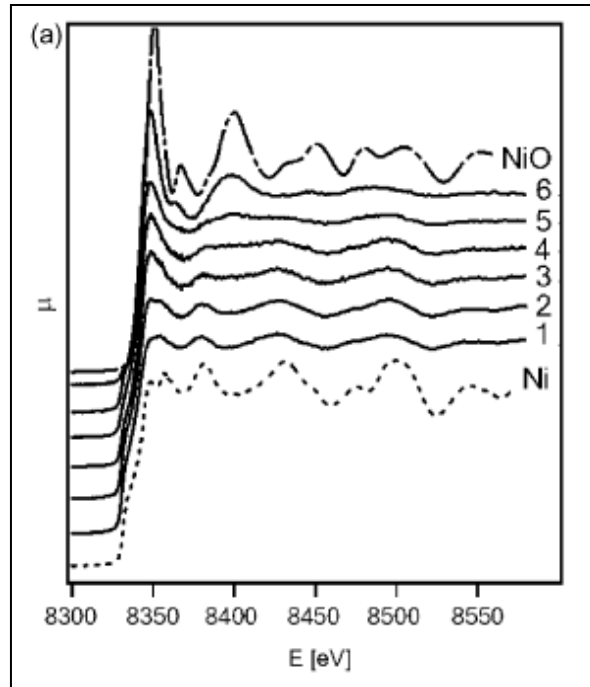


Figure 36. XAFS spectra obtained from composite material published by Nietubyc et al. The top and bottom lines show NiO and Ni spectra respectively. The intermediate lines show results from samples with varying levels of NiO, from most (top) to least (bottom).

4.4.3 Theoretical Fits

Data was compared to theoretical models via multiple scattering calculations computed using the Athena and Artemis XAFS analysis programs. In order to do so, a pre-absorption edge line was regressed and subtracted from the data. Then a post edge step line was regressed, and the pre edge line was subtracted from the post edge line to obtain the edge step parameter. All data were divided by the edge step parameter to normalized the data. Finally, the data were Fourier transformed from energy space to K space, then converted to R space. Plotting in R space provides a quick way of examining

bond lengths and thus identifying potential contributors to the XAFS oscillations. Figure 37 shows all the sample data plotted in R space.

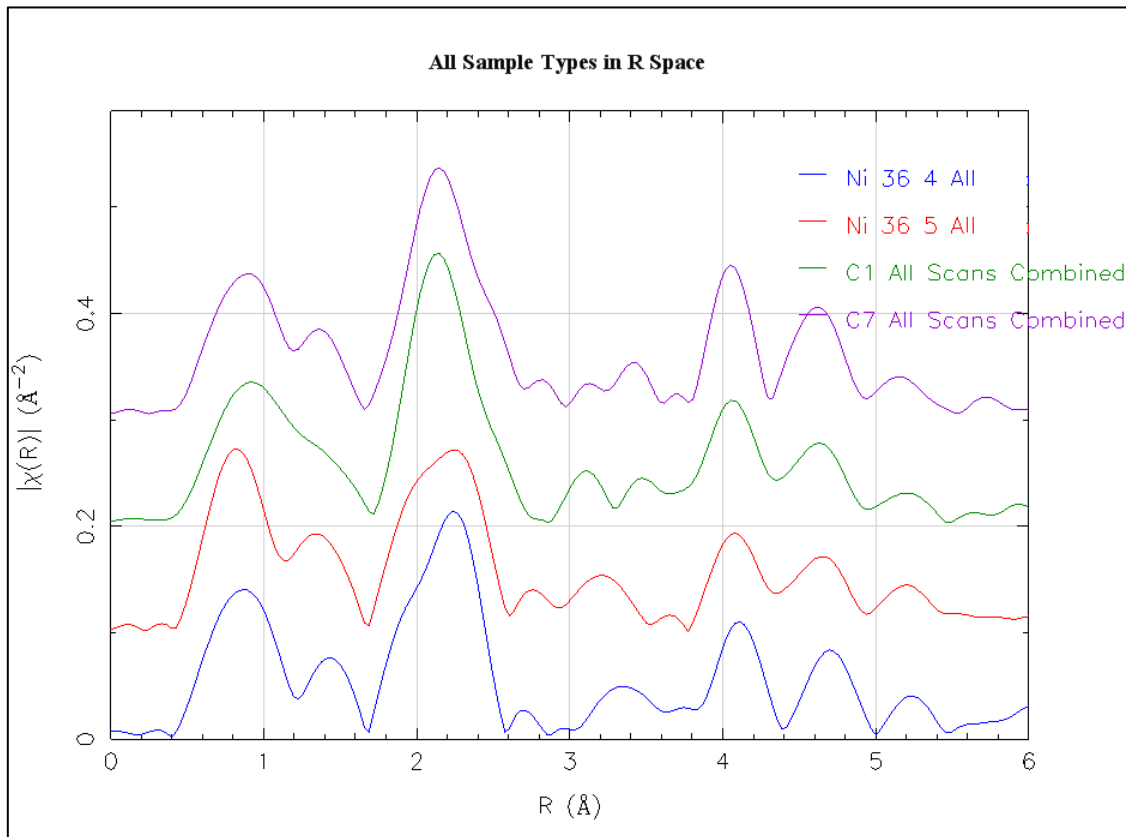


Figure 37. XAFS data plotted in R-space.

Once the data had been converted to R space, theoretical models were fitted to the data. Crystallographic models for nickel, carbon, nickel-oxide, and nickel-hydroxide were used, and it was assumed that the recorded signal was some linear combination of those materials. Contributions from the polymer were ignored. Fittings were done by conducting multiple scattering calculations from the crystallographic models and comparing them to the measurement data. For the fits, only path lengths shorter than

2.585 Å were considered, as that was the apparent maximum extent of the first shell based on the plots in R space. Previous studies suggested that fitting the second and third

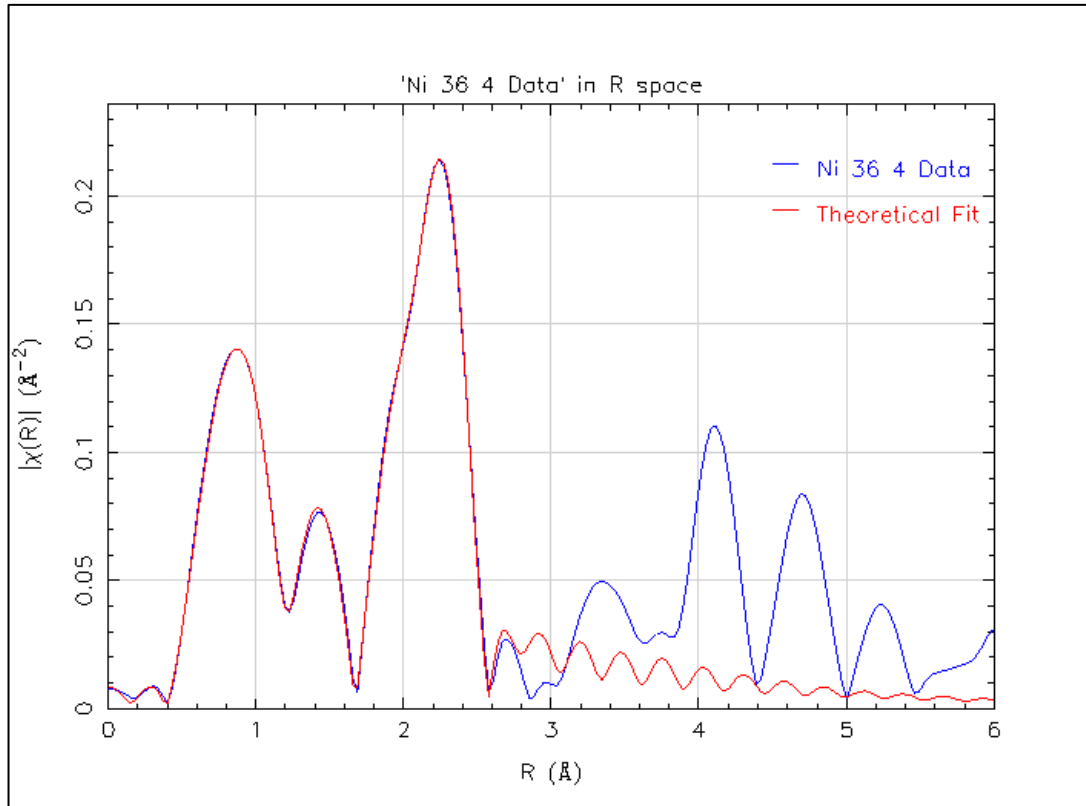


Figure 38. Curve fitting results for sample Ni-36-4. Only the first shell was fitted.

shells would be result in large uncertainties, moreover the known bond lengths for nickel-nickel and nickel-oxide bonds were less than 2.585Å at 2.49 Å and 2.08 Å respectively [20]. An example of the curve fitting results is presented in Figure 37. Fitting was conducted for each possible combination of the four material types, and in all cases the best fit was found for combinations of all four materials, although the contribution to the signal from NiOH was always found to be very small or negligible. Table 10 shows the contributions that were found. Note, however that the relative contributions to the fitting

in R space do not directly translate to percent material present in the sample. For comparison, the spectrum labeled 3 in Figure 36 was obtained for a sample composed of 18% nickel-oxide and 82% nickel.

As is shown in Table 10, the contributions from NiO were smaller in irradiated samples, C1 and Ni-36-4, than in the corresponding non-irradiated samples, C7 and Ni-36-5, which indicated lower oxide content in the irradiated samples. This matched the results from the surface resistivity measurements.

Table 10. Calculated contributions to the XAFS signal from each sample showing nickel, carbon, nickel-oxide, and nickel-hydroxide relative contributions.

Sample	Irradiation Level [cm ⁻²]	Nickel %	Carbon %	NiO %	NiOH %
C1	2 x 10 ¹⁶	51.9	27.8	20.4	0.0
C7	0	13.5	41.4	44.4	0.8
Ni 36 4	2 x 10 ¹⁶	43.9	29.3	26.8	0.0
Ni 36 5	0	25.4	29.9	44.8	0.0

V. Conclusions and Recommendations

In conclusion, pre and post irradiation resistivity and XAFS measurements were conducted to examine the effects of 0.5 MeV electron irradiation on nickel-carbon composites. Results showed a decrease in surface resistivity and a corresponding decrease in NiO content for the irradiated samples as compared to pre-irradiation measurements and non-irradiated samples. Surface resistivity measurement capabilities were established and measurement techniques refined. Measured changes in surface resistivity were not consistent with previous results, but were consistent with studies on the radiation effects on electrical properties of polymers similar to the epoxies used in fabricating the composites. Moreover, higher fluence levels were required to achieve measurable results compared with previous research, indicating that the materials examined showed radiation tolerance to energetic electrons. The data showed no discernable link between irradiation changes to surface resistivity and epoxy type used. Further studies are required to develop more reliable bulk resistivity measurements so that changes in bulk resistivity can be discerned and compared with changes in surface resistivity.

The differences in true surface resistivity found using two separate correction methods, the infinite bar approximation and the finite element analysis, indicated that further work is needed to better model the current flow through these composite materials. It is believed that small changes in sample placement on the four probe sample holder may result in current flowing through entirely different paths. Charge flow in surface resistivity measurements is expected to have some penetration depth into the

material, perpendicular to the surface. Given the non-homogeneous nature of these materials, that is likely a complex process which merits further investigation. It would be worthwhile to develop a finite element model of the specific composite samples used in this investigation and model the current flow in a linear 4-point setup. The model could be compared to a homogeneous material to provide additional insight into the current flow and possibly changes to current flow following irradiation.

The finding that measured changes in surface resistivity was greater for the sample sides facing the beam suggests that further investigation is also needed to better understand how energy transfer between the radiation and the material leads to changes in electrical properties. CASINO[®] simulations had indicated energy deposition would be greatest on the sides facing away from the electron beam. Additional tests should be conducted to determine if the simulations were inaccurate. Such measurements could also be performed using electron irradiation of varying energies, which would enable exploration of the possibility that knock-on damage or another energy dependent mechanism is responsible for the different magnitude of changes measured between the two sides of the samples. Finally, improvements to the surface resistivity setup should be made to reduce measurement variation. A modification to the HDPE sample holder could be made to restrict the lateral placement of the sample without contacting the conductive retaining bolts. This could reduce measurement variation so that detecting changes would be possible for fluence levels below $2 \times 10^{16} \text{ cm}^{-2}$.

Conductive composites can be an excellent choice for applications that require strong, lightweight, low resistance materials. Moreover, the materials investigated here

have shown the ability to retain electro-magnetic properties following exposure to a radiation environment with all measured changes less than 30%. However, the results of this investigation highlight the need to conduct additional research in order to develop a better understanding of charge conduction through these materials and the fundamental changes that take place following irradiation.

Appendix A Pre-Irradiation Surface Resistivity Measurements

Table 11. Pre-irradiation surface resistivity measurement results showing resistance values averaged from 3 measurements and the corresponding standard deviations.

Pre Irradiation Surface Resistivity Measurements Set 1			
Sample	Dot Alignment	Average Resistance Measured [mΩ]	Standard Deviation [mΩ]
Ni-36-1	up	136	4
Ni-36-1	down	156	5
Ni-36-2	up	131	2
Ni-36-2	down	155	10
Ni-36-3	up	143	8
Ni-36-3	down	172	21
Ni-36-5	up	147	10
Ni-36-5	down	136	9
Ni-36-6	up	144	5
Ni-36-6	down	160	1
C-36-1	up	182	5
C-36-1	down	167	2
C-36-2	up	184	3
C-36-2	down	169	2
C-36-3	up	151	2
C-36-3	down	167	2
Ni-3-1	up	195	3
Ni-3-1	down	182	1
Ni-3-2	up	172	1
Ni-3-2	down	133	1
Ni-3-3	up	136	3
Ni-3-3	down	175	1
C-3-1	up	N/A	N/A
C-3-1	down	N/A	N/A
C-3-2	up	N/A	N/A
C-3-2	down	N/A	N/A
C-3-3	up	N/A	N/A
C-3-3	down	N/A	N/A

Table 12. Surface resistivity measurement results showing resistance values averaged from 20 measurements and 68% confidence interval from best fit distribution. Note, Ni-36, C-36, and Ni-3 samples were all measured after irradiation to $2 \times 10^{16} \text{ cm}^{-2}$

Surface Resistivity Measurements Set 2				
			68% Confidence Interval	
Sample	Dot Alignment	Average Measured Resistance [$\text{m}\Omega$]	Minimum [$\text{m}\Omega$]	Maximum [$\text{m}\Omega$]
Ni-36-1	up	129	125	136
Ni-36-1	down	166	154	175
C-36-2	up	154	153	155
C-36-2	down	142	140	145
Ni-3-1	up	168	165	171
Ni-3-1	down	162	158	166
C-3-3	up	284	262	316
C-3-3	down	198	196	201

Bibliography

- [1] G. Hansen, "High Aspect Ratio Sub-Micron and Nano-scale Metal Filaments," *SAMPE Journal*, 41(2), pp. 2-11, Mar. 2005.
- [2] T. F. Tascione, *Introduction to the Space Environment*, Malabar: Krieger Publishing Company, 1994, pp. 133-135
- [3] Metal Matrix Composites Corp. LLC, "Nanostrands: 'Nickel at Its Finest'," 2004, <http://www.nanostrands.com>.
- [4] J. D. McGary, "Electrostatic Discharge Properties of Irradiated Nanocomposites," M.S. Thesis, 1-97, Air Force Institute of Technology, Wright-Patterson AFB, 2009.
- [5] J. D. McGary et al., "Electrostatic Discharge Properties of Irradiated Nanocomposites," Unpublished, 2009, pp. 1-4.
- [6] NASA website http://imagine.gsfc.nasa.gov/docs/ask_astro/answers/970408d.html
- [7] T. Berger "The Space Radiation Environment," website <http://www.ati.ac.at/~vanwaweb/spacerad.html>
- [8] MIL-STD-1809, United States Air Force, "Space Environment for USAF Space Vehicles," February 15, 1991, pp. 20-23.
- [9] M.A. Heald and J.B Marion, *Classic Electromagnetic Radiation*, Boston: Thomas Learning Inc, 1995, pp. 127-130.
- [10] B. T. Harder, "Evaluation of Nanocomposites as Lightweight Electronic Enclosures for Satellites' Applications," M.S. Thesis, Air Force Institute of Technology, Wright-Patterson AFB, 2008, pp. 1-40.
- [11] A. Charlesby, *Atomic Radiation and Polymers*, New York: Pergamon Press, 1960, pp. 18-40.
- [12] A. Tyutnev, R Ikhsanov, V. Saenko, and E. Pozhidaev, "Theoretical Description of the Prompt Component of Pulsed Radiation-Induced Conductivity in Polymers in Terms of the Ion Pair Mechanism of Radiolysis," *High Energy Chemistry*, 42(4), pp. 308-313.

- [13] A. Chapiro, *Radiation Chemistry of Polymeric Systems*, 349, New York: John Wiley and Sons, 1962, pp. 40-49.
- [14] C. Hanks and D. Hamman, "Radiation Effects Design Handbook," NASA Contractor Report 1787 Section 3, NASA, 1971, pp. 22-23.
- [15] A. Dannoux, S. Esnouf, B. Amekraz, V. Dauvois, C. Moulin. "Degradation Mechanism of Poly(ether-urethane) Estane[®] Induced by High-Energy Radiation," *Journal of Polymer Science: Part B: Polymer Physics*, Vol. 46, pp. 861-878, 2008.
- [16] M. Van de Voorde and C. Restat, "Selection guide to organic materials for nuclear engineering," CERN Report, 72(7), pp. 10-14, 1972.
- [17] H. Schonbacher and A. Stolarz-Izycka, "Compilation of radiation damage test data: cable insulating materials. Index des resultants d'essais de radiorsistance: Matriaux d'isolation de cables," CERN 98-01, 1998.
- [18] M. Tavlet, "Radiation in Hadron Accelerators and their Effects on Materials," <http://at-hhh-amt.web.cern.ch/AT-HHH-AMT/Presentations/Tavlet.pdf>, March 2005.
- [19] P. Young, W. Slempe, and B. Stein, "Performance of Selected Polymeric Materials on LDEF: N94-31023," Hampton: NASA Langley Research Center, 1994, pp. 125-142.
- [20] M. Ushiro, K. Uno, T. Fujikawa, et al., "X-ray absorption fine structure (XAFS) analyses of Ni species trapped in grapheme sheet of carbon nanofibers," *Physical Review B*, 73, pp. 144103-10, 2006.
- [21] R. Nietubyc, E. Czerwosz, R. Diduszko, et al., "XAFS studies of the short-range order in Ni nanoparticles embedded in carbonacoues matrix," *Journal of Alloys and Compounds*, 19972, pp. 1-6, 2009.
- [22] M. Newville, "Fundamentals of XAFS," Chicago: University of Chicago, 2004.
- [23] NIST, "XCOM: Photon Cross Section Database," <http://physics.nist.gov/PhysRefData/Xcom/Text/XCOM.html>.
- [24] E Zimney, G Dommett, R Ruoff, and D Dikkin, "Correction factors for 4-probe electrical measurements with finite size electrodes and material anisotropy: a finite element study," *Measurement Science and Technology*, 18, pp. 2067-2073, 2007.

- [25] W.A. Taylor, "Distribution Analyzer User's Guide," Libertyville: Taylor Enterprises Inc., 2007, pp. 60-91.
- [26] S. Pierpoint, J. Silverman, M. Al-Sheikhly, "Effects of ionizing radiation on the aging of polyester based polyurethane binder," *Radiation Physics and Chemistry* 62: pp. 163-169, 2001.
- [27] B Ravat et al., "Electron irradiation of polyurethane: Some FTIR results and a comparison with a EGS4 simulation," *Nuclear Instruments and Methods in Physics Research B* 160, pp. 499-504, 2000.
- [28] H. Gumus and O Kabadayi, "Z2 structure of the stopping power for electron beams," *Nuclear Instruments and Methods in Physics Research B* 267, pp. 299-301, 2009.
- [29] Haldor Topsoe Semiconductor Division, "Geometric factors in four point resistivity measurement," Vedbaek: Haldor Topsoe, 1968, pp. 31-33.

REPORT DOCUMENTATION PAGE				<i>Form Approved OMB No. 074-0188</i>	
<p>The public reporting burden for this collection of information is estimated to average 1 hour per response, including the time for reviewing instructions, searching existing data sources, gathering and maintaining the data needed, and completing and reviewing the collection of information. Send comments regarding this burden estimate or any other aspect of the collection of information, including suggestions for reducing this burden to Department of Defense, Washington Headquarters Services, Directorate for Information Operations and Reports (0704-0188), 1215 Jefferson Davis Highway, Suite 1204, Arlington, VA 22202-4302. Respondents should be aware that notwithstanding any other provision of law, no person shall be subject to a penalty for failing to comply with a collection of information if it does not display a currently valid OMB control number. PLEASE DO NOT RETURN YOUR FORM TO THE ABOVE ADDRESS.</p>					
1. REPORT DATE (DD-MM-YYYY) 25-03-2010		2. REPORT TYPE Master's Thesis		3. DATES COVERED (From - To) July 2009 – March 2010	
4. TITLE AND SUBTITLE Changes to Electrical Conductivity in Irradiated Carbon-Nickel Nanocomposites				5a. CONTRACT NUMBER	
				5b. GRANT NUMBER	
				5c. PROGRAM ELEMENT NUMBER	
6. AUTHOR(S) Coy, David F., Major, USA				5d. PROJECT NUMBER	
				5e. TASK NUMBER	
				5f. WORK UNIT NUMBER	
7. PERFORMING ORGANIZATION NAMES(S) AND ADDRESS(S) Air Force Institute of Technology Graduate School of Engineering and Management (AFIT/EN) 2950 Hobson Way, Building 640 WPAFB OH 45433-8865				8. PERFORMING ORGANIZATION REPORT NUMBER AFIT/GNE/ENP/10M-02	
9. SPONSORING/MONITORING AGENCY NAME(S) AND ADDRESS(ES) intentionally left blank				10. SPONSOR/MONITOR'S ACRONYM(S)	
				11. SPONSOR/MONITOR'S REPORT NUMBER(S)	
12. DISTRIBUTION/AVAILABILITY STATEMENT APPROVED FOR PUBLIC RELEASE; DISTRIBUTION UNLIMITED.					
13. SUPPLEMENTARY NOTES					
14. ABSTRACT Pre and post irradiation resistivity and XAFS measurements have been conducted to examine the effects of 0.5 MeV electron irradiation on nickel-carbon composites. Results showed a decrease in surface resistivity following irradiation and a corresponding decrease in NiO content for the irradiated samples as compared to pre-irradiation measurements and non-irradiated samples. Surface resistivity measurement capabilities were established and measurement techniques refined to produce repeatable results of sufficient precision to discern changes in resistivity for fluence levels of $2 \times 10^{16} \text{ cm}^{-2}$ and greater. Measured changes in surface resistivity were found to be consistent with studies on the radiation effects on electrical properties of polymers similar to the epoxies used in fabricating the composites studied here. The materials examined showed changes of 30% or less following irradiation with 0.5 MeV electrons to a total electron fluence of to $4 \times 10^{16} \text{ cm}^{-2}$. The data showed no discernable link between irradiation changes to surface resistivity and epoxy type used.					
15. SUBJECT TERMS Conductive composites, radiation effects					
16. SECURITY CLASSIFICATION OF:			17. LIMITATION OF ABSTRACT	18. NUMBER OF PAGES	19a. NAME OF RESPONSIBLE PERSON
a. REPORT	b. ABSTRACT	c. THIS PAGE			19b. TELEPHONE NUMBER (Include area code)
U	U	U	UU	100	Dr. James C. Petrosky (937) 255-6565, ext 4562 (emailname@afit.edu)

